



저작자표시-비영리-변경금지 2.0 대한민국

이용자는 아래의 조건을 따르는 경우에 한하여 자유롭게

- 이 저작물을 복제, 배포, 전송, 전시, 공연 및 방송할 수 있습니다.

다음과 같은 조건을 따라야 합니다:



저작자표시. 귀하는 원저작자를 표시하여야 합니다.



비영리. 귀하는 이 저작물을 영리 목적으로 이용할 수 없습니다.



변경금지. 귀하는 이 저작물을 개작, 변형 또는 가공할 수 없습니다.

- 귀하는, 이 저작물의 재이용이나 배포의 경우, 이 저작물에 적용된 이용허락조건을 명확하게 나타내어야 합니다.
- 저작권자로부터 별도의 허가를 받으면 이러한 조건들은 적용되지 않습니다.

저작권법에 따른 이용자의 권리는 위의 내용에 의하여 영향을 받지 않습니다.

이것은 [이용허락규약\(Legal Code\)](#)을 이해하기 쉽게 요약한 것입니다.

[Disclaimer](#)

공학박사 학위논문

**Nanostructured WC–Co Powders and
Bulks via Integrated Mechanical/Thermal
Activation and Liquid Phase Sintering**

기계적/열적 활성화 및 액상 소결을 통한
WC 나노 분말 및 WC–Co 나노 복합체 제조

2 0 1 7 년 8 월

서울대학교 대학원

재료공학부

박 충 권

Ph. D. Dissertation

**Nanostructured WC–Co Powders and Bulks via
Integrated Mechanical/Thermal Activation and
Liquid Phase Sintering**

A dissertation Submitted in fulfilment of the requirements for the
degree of Doctor Philosophy

Approved by Major Advisor

2017. 08

**Department of Materials Science and Engineering
Seoul National University**

Choong Kwon Park

**Nanostructured WC-Co Powders and Bulks via
Integrated Mechanical/Thermal Activation and Liquid
Phase Sintering**

지도교수 강 신 후

이 논문을 공학박사학위논문으로 제출함

2017년 8월



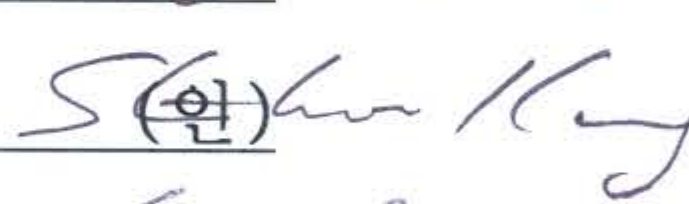
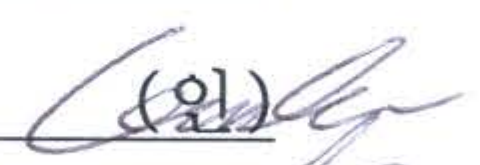
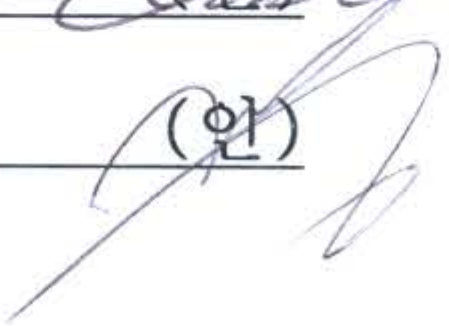
서울대학교 대학원

재료공학부

박 충 권

박 충 권의 박사학위논문을 인준함

2017년 8월

위원장	박 찬	(인) 
부위원장	홍 성 현	(인) 
위원	강 신 후	(인) 
위원	이 관 형	(인) 
위원	김 지 웅	(인) 

Abstract**Nanostructured WC–Co Powders and Bulks via
Integrated Mechanical/Thermal Activation and
Liquid Phase Sintering**

Choongkwon Park

Dept. of Material Science & Engineering

The Graduate School

Seoul National University

WC–Co composites have been widely used as a cutting tools, saw blade, dies and valves in industrial fields where high hardness, toughness and wear resistant properties are required. Due to the strategic importance of the resources for WC–Co composites, substantial research efforts have been directed towards the synthesis of WC nanopowder and nanostructured WC–Co composites in order to enhance further their mechanical properties and lifetimes. Nonetheless, the specification of mass production type of WC–Co composites is now limited to the average particle size of > 200 nm. In this thesis, we suggest a scalable production pathway for an extremely fine WC nanopowder (10.54 nm) and a genuine nanostructured WC–Co composites (20~30 nm).

First, we systematically studied the mechanism for the reactions and growth of reactants during carbothermal reduction with the experimental and

theoretical approaches. The results reveal that the finer the intermediates is, the faster the reactions, the lower the reaction temperature becomes. All the processes during carbothermal reduction are governed by the diffusion of constituent elements. Based on these findings, we successfully synthesized an extremely fine WC nanopowder with an average size of 10.54 nm with a standard deviation of 2.1 nm.

Second, we investigated the mechanism for the grain growth inhibition during liquid phase sintering, and suggest the possibilities for the production of nanostructured WC–Co composites with an average grain size of 30 nm. By the addition of VC, an extremely unstable nanostructure of WC–Co is found to have a significantly high thermal stability and an unusual microstructure. The nanostructure with carbide size less than 30 nm was retained for a long time (1h) up to 1300 °C. The growth of WC in the system is limited by two-dimensional nucleation of WC on (V,W)C layer and consequent diffusion of W through the layer. The high thermodynamic stability of the nanostructure assures the realizable possibility of the mass production of a genuine nanostructured WC–Co composites.

Keywords : Nanostructure, WC-VC-Co, grain growth inhibition, twinning in nanostructure, HRTEM

Student Number : 2010-24047

Contents

Abstract	i
Contents.....	iii
List of Table Captions	vi
List of Figure Captions.....	vii
Part I	10
I. Introduction.....	11
1.1 Synthesis of WC nanopowder.....	11
1.2 Purpose of the work.....	14
II. Experimental procedure.....	15
2.1 Materials and methods.....	15
2.2 Characterization.....	16
III. Result and discussion.....	17
3.1 Reactions of $\text{WO}_3\text{--C}$ mixture during carbothermal reduction	17
3.2 Grain growth of intermediates during carbothermal reduction	34
3.3 Synthesis of Nanopowders via grain growth controlled method.....	44
IV. Conclusion.....	47

Part II	48
I. Introduction	49
1.1 Mechanism of grain growth inhibition of WC during Liquid Phase Sintering	49
1.2 Synthesis of nano WC-Co composites via liquid phase sintering.....	52
1.3 Purpose of the work.....	55
II. Experimental procedure	56
2.1 Materials and methods.....	56
2.2 Characterization.....	58
III. Result and discussion	59
3.1 WC growth in undoped WC–Co.....	59
3.2 Particle growth of VC-doped WC–Co	64
3.3 Interface characterization: (V,W)C cubic layer formation	66
3.4 Formation of Twins and Ledges.....	70
3.5 Effect of Step Free Energy.....	74
3.6 Effect of Solubility and Diffusivity of W.....	76
3.7 Effect of Interfacial Energy.....	77
3.8 Modeling of particle growth of VC-doped WC–Co system.....	78
3.9 Synthesis of nano WC-Co via liquid phase sintering.....	83
IV. Conclusion	87
Overall Conclusion	88
Reference	90
Abstract (Korean)	98

Contents

v

Further Works.....

100

Curriculum Vitae.....

101

Acknowledgement.....

104

List of Tables

TABLE 1. THE SUMMARIZATION OF WC NANOPOWDER PROCESSING TECHNIQUES.....	13
TABLE 2. THE PHASE CONSTITUTIONS AND THEIR XRD PEAK SHARPNESS OF WO ₃ -C MIXTURE WITH TEMPERATURE AND HEATING RATE.....	25
TABLE 3. THE SUMMARIZATION OF THE RESULTS RELATED TO THE SINTERING OF THE NANOSTRUCTURED WC-Co COMPOSITES FROM LITERATURE[1, 59].	53

List of Figures

FIGURE 1. TGA/DSC CURVES FOR WO ₃ -C MIXTURE MILLED FOR 30 H. THE BLACK LINE INDICATES THE TGA CURVE AND THE RED LINE SHOWS DSC CURVE.	17
FIGURE 2. XRD PATTERNS OF WO ₃ -C MIXTURE AT DIFFERENT TEMPERATURES DURING CARBOTHERMAL REDUCTION.	19
FIGURE 3. THE VARIATION OF GIBBS FREE ENERGY WITH TEMPERATURE FOR THE REACTIONS DURING CARBOTHERMAL REDUCTION PROCESS OF WO ₃ -C MIXTURE..	21
FIGURE 4. XRD PATTERNS OF WO ₃ -C MIXTURE WITH TEMPERATURE AND HEATING RATE. (A) 20 K/MIN, (B) 5 K/MIN.	23
FIGURE 5. (A-C) FESEM MICROGRAPHS OF AS-MILLED WO ₃ -C MIXTURE (A), THE SAMPLE HEATED TO 1373 K AT 10 K/MIN (B) AND THE SAMPLE HEATED TO 1473 K AT 20 K/MIN (C). (D) THE MEASURED GRAIN SIZE DISTRIBUTIONS FOR THE SAMPLES.	27
FIGURE 6. HR-TEM MICROGRAPHS OF WO ₃ -C MIXTURES HEATED TO 1273 K FOR TWO DIFFERENT HOLDING TIMES. (A) FOR 10 MIN AND (B) FOR 60 MIN.	29
FIGURE 7. SCHEMATIC ILLUSTRATION OF THE REDUCTION AND CARBURIZATION OF WO ₃ PARTICLES BY CARBON.	29
FIGURE 8. SCHEMATIC ILLUSTRATION OF THE SPHERICAL DIFFUSION MODEL IN A STEADY-STATE.	30
FIGURE 9. THE VARIATION OF $(r/R)^3$ WITH TIME, TEMPERATURE AND THE SIZE OF W ₂ C GRAIN, R.	33
FIGURE 10. THE VARIATION OF THE AVERAGE GRAIN SIZE OF WC AS A FUNCTION OF TIME AT 1100 AND 1200 °C.	34
FIGURE 11. THE VARIATION IN THE CUBE OF THE AVERAGE GRAIN SIZE OF WC POWDER WITH HOLDING TIME (T) AT 1100 AND 1200 °C, RESPECTIVELY.	35
FIGURE 12. FESEM (A) AND TEM (B) MICROGRAPHS FOR THE WC POWDER SAMPLE HEATED TO 1473 K AT A HEATING RATE OF 20 K/MIN.	36
FIGURE 13. TWO PARTICLE MODEL FOR THE FORMATION OF NECK INVOLVING SHRINKAGE DURING CARBOTHERMAL REDUCTION REACTION.	37
FIGURE 14. THE SCHEMATIC PRESENTATION OF VARIOUS DIFFUSION PATHS CONTRIBUTED TO THE GROWTH OF NECK.	38
FIGURE 15. SCHEMATIC PRESENTATION OF THE GRAIN GROWTH DURING CARBOTHERMAL REDUCTION THROUGH THE DIFFUSION OF SURFACE AND THE DIFFUSION PERPENDICULAR TO THE GRAIN BOUNDARY.	40

- FIGURE 16. FESEM IMAGES FOR THE NANOPOWDERS SYNTHESIZED VIA GRAIN GROWTH CONTROLLED METHOD. (A) WC (10 NM), (B) VC (30 NM), (C) TiC (50 NM), (D) $(\text{Ti}_{0.88}\text{W}_{0.12})\text{C}$ (30 NM), (E) Co (20 NM), (F) Ni (20 NM).....44
- FIGURE 17. FESEM, DF-TEM IMAGES AND THE GRAIN SIZE DISTRIBUTION OF WC NANOPOWDER SYNTHESIZED VIA THE GRAIN GROWTH CONTROLLED METHOD.46
- FIGURE 18. FESEM MICROGRAPHS AND GRAIN SIZE DISTRIBUTION FOR PURE WC–CO SAMPLES SINTERED AT TWO REPRESENTATIVE TEMPERATURES AND TIMES. A FAST HEATING RATE OF 300 °C/MIN WAS EMPLOYED IN ORDER TO MINIMIZE THE GRAIN GROWTH DURING HEATING: (A) 1250 °C FOR 1 MIN (B) 1350 °C FOR 1 MIN, (C) THE PARTICLE SIZE DISTRIBUTION ALONG WITH THE AVERAGE SIZE.60
- FIGURE 19. SCHEMATIC ILLUSTRATION OF THE CRITICAL DRIVING FORCES AT 1250 AND 1350 °C AND THE DRIVING FORCES OF THE LARGEST GRAINS AT THE TEMPERATURES AND DURATION TIMES, $\Delta g_{LGT} - t$, ALONG WITH THE GRAIN GROWTH RATES WITH THE DRIVING FORCES.....63
- FIGURE 20. . FESEM IMAGES AND GRAIN SIZE DISTRIBUTION FOR THE VC-DOPED WC–CO SAMPLES SINTERED AT VARIOUS TEMPERATURES AND TIMES. SLOW HEATING RATE OF 10 °C/MIN WAS EMPLOYED IN ORDER TO MAXIMIZE THE EFFECT OF GRAIN GROWTH INHIBITION: (A) 1250 °C FOR 1 H, (B) 1300 °C FOR 1 H, (C) 1350 °C FOR 1 H. (D), (E) AND (F) SHOW THE VARIATION OF THE PARTICLE SIZE DISTRIBUTION AT 1250, 1300 AND 1350 °C, RESPECTIVELY, AS A FUNCTION OF TIME. THE GRAINS WITH FACETED INTERFACES ARE MARKED BY WHITE ARROWS.....65
- FIGURE 21. CS-STEM MICROGRAPHS OF VC-DOPED WC–CO SAMPLE PREPARED BY QUENCHING FROM 1200 °C AFTER 1 H SINTERING: (A) STEM DARK-FIELD (DF) IMAGE SHOWING WC GRAIN ANALYZED, (B) HIGH RESOLUTION (HR) STEM DF IMAGE ILLUSTRATING THE SEGREGATED (V,W)C ATOMIC LAYERS ON 1010 SURFACE OF WC IN THE REGION LABELED A, (C) HR STEM BRIGHT-FIELD (BF) IMAGE SHOWING THE THE SEGREGATED (V,W)C ATOMIC LAYERS ON 0001 SURFACE OF WC IN THE REGION LABELED B. (D) AND (E) ILLUSTRATE THE ORIENTATION RELATIONSHIP AT THE PRISMATIC AND BASAL INTERFACES, RESPECTIVELY.....68
- FIGURE 22. CS-STEM MICROGRAPHS OF VC-DOPED WC–CO SAMPLE PREPARED BY QUENCHING FROM 1200 °C AFTER 1 H SINTERING; (A) STEM BF IMAGE SHOWING WC GRAINS WITH A HIGH DENSITY OF TWINS, (B) AND (C) HR STEM DF IMAGE ILLUSTRATING THE ARRAY OF TWINS INSIDE WC GRAIN AND LEDGES ON THE SURFACE OF GRAIN. (D) AND (E) ARE HR STEM DF IMAGE AND EDS RESULT, RESPECTIVELY, SHOWING THE PRESENCE OF V AND THE ORIGIN OF TWINS. (F)

DEMONSTRATES THE TRAPPED V CLUSTER AND (G) PROVIDES AN EVIDENCE FOR THE V OR W DIFFUSION THROUGH (V,W)C CUBIC LAYERS. YELLOW ARROWS INDICATE THE TWINS AND WHITE DASHED ELLIPSES THE LEDGES ON THE PRISMATIC FACETS IN (B) AND (C). PINK ELLIPSES IN (D), (F) AND (G) ARE FOR V ATOM AND CLUSTERS TRAPPED IN WC GRAIN.	71
FIGURE 23. THE ESTIMATED NUMBERS OF WC GRAINS PER UNIT VOLUME AND THE NUMBERS OF WC GRAINS PER UNIT VOLUME, WHICH CAN BE COVERED BY (V,W)C CUBIC LAYERS, WITH GRAIN SIZE. (A) SCHEMATIC DIAGRAM OF WC GRAIN, (B) THE CALCULATED RESULTS.	79
FIGURE 24. SCHEMATIC ILLUSTRATION OF THE CONCENTRATION PROFILE OF W THROUGH THE PHASES AND 2-DN ON (V,W)C LAYER, THROUGH WHICH W DIFFUSION OCCURS.....	80
FIGURE 25. THE VARIATION OF THE RELATIVE DENSITIES AND WC PARTICLE SIZES WITH TEMPERATURE AND TIME DURING LIQUID PHASE SINTERING.....	84
FIGURE 26. FESEM MICROGRAPHS FOR THE SAMPLES SINTERED AT 1250 (A), 1300 (B) AND 1350 °C (C) FOR 1H, RESPECTIVELY.	84
FIGURE 27. FESEM MICROGRAPH OF THE SAMPLE HEATED TO 1300 °C AT A HEATING RATE OF 100 °C/MIN AND HELD AT THE TEMPERATURE FOR 1 MIN.	85

Part I

Synthesis of WC Nanopowder

I. Introduction

1.1. Synthesis of WC nanopowder

Nanostructured WC–Co materials have long been the main subject of interests and focus of research programs around the world in common with other structural material and functional material fields [1]. Extremely fine microstructures with nanoscale grain size have the potential to dramatically improve both their hardness and toughness simultaneously. When the size of dispersoids reach to a critical size range (5-30 nm), a significant improvement in both hardness and toughness is anticipated from the theory of dispersion strengthening. The improvements and nanostructures are particularly beneficial for not only the lifetime and robustness of WC–Co tools [1] but also the micro-drills for printed circuit boards manufacture [2]. This industrial significance drives the intensive research activities towards the production of genuine nanostructured WC–Co (<100 nm).

In order to realize the production of the nanostructured WC–Co composites, the effective production of WC nanopowder has a first importance. Many powder production technologies ranged from conventional solid state synthesis to more radical techniques such as high energy ball milling [3-8], integrated mechanical and thermal activation (IMTA) [9-11], spray conversion [12-19], chemical vapor phase reaction [20-28] and microwave synthesis [29] have been introduced, which are summarized in Table 1. Although many of these techniques were employed, the mass production of WC nanopowders with an extremely fine grain size of less than 100 nm is still difficult as listed in Table

1. A mechanical milling techniques such as high energy ball milling is most effective for the reduction of grain size, but these processes cannot be applied for the mass production because these processes suffer from the drawbacks of long processing times, contamination and high energy expenditures[3-8]. Although except for mechanical milling, the other techniques listed in Table 1 are feasible for the mass production, the grain growth is inevitable during production processes because they involve a heat treatment at high temperature for a long time. Therefore, understanding the underlying mechanisms of the reactions and growth during powder production process is instructive for a better control over grain growth and successive production of nanopowder with an extremely fine grain size.

Table 1. The summarization of WC nanopowder processing techniques.

Powder production process	Process condition				Grain size (nm)	Pros	Cons	Mass production feasibility	Reference
	Raw materials	Methods	condition	Equipment					
Mechanical ball milling	Micron-sized WC powder	Top down	>100 h	Planetary/attrition /high energy dual-drive planetary mill	10–20	Effective size reduction	Long processing time/contamination	Not favorable	[3-8]
Mechanochemical synthesis	WO ₃ , graphite, Mg, HCl	Top down	250 rpm–50 h	Planetary ball mill	4–20	Effective size reduction	–	Not favorable	[30]
	W, graphite	Top down	250 rpm–450 Ks	Planetary ball mill	5	Effective size reduction	–	Not favorable	[31]
IMTA	WO ₃ , graphite, Co	Top down	600 rpm–12 h, 1000 °C–2 h	Planetary ball mill/furnace	30–100	Effective size reduction	Low cost	Possible	[9, 10]
Spray conversion process	Soluble precursor	Bottom up	–	Aqueous solution formation/spray drying/carburization	20–50	Effective size reduction	Long processing time	Possible	[12-19]
Chemical vapor phase reaction	WCl ₆ /WF ₆ /W (CO) ₆ , H ₂ (g), CH ₄ (g)/C ₃ H ₈ /C ₂ H ₂	Bottom up	1000–1400 °C	CVS Reactor	40–1000	High purity/good control for size, reaction rate	–	Possible	[20-28]

1.2. Purpose of the work

In this part, we developed the methodology for the synthesis of an extremely fine WC nanopowder using IMTA method with an in-depth study for the underlying mechanisms of the formation of WC during carbothermal reduction.

IMTA method was employed in this work because it is not only feasible for the mass production of nanocrystalline WC powders, but also typical that raw materials experience the various reductions and grain growth during process. The focus is on the reactions and growth during heating stage of carbothermal reduction process. Although synthesis of WC nanopowder have been intensively studied during past several decades, the successive mass production of an extremely fine WC nanopowder (<50 nm) is still not realized, which might be due to the lack of the understanding for the underlying mechanism of the reactions and growth during process. The present work investigated the formation mechanism of WC during carbothermal reduction of $\text{WO}_3\text{-C}$ powder mixture and suggests the grain growth controlled production method of WC nanopowder with an extremely fine grains size of <20 nm.

II. Experimental procedure

2.1. Materials and methods

Tungsten trioxide powder (particle size: $\leq 20\text{ }\mu\text{m}$; purity: 99%; Sigma-Aldrich, St. Louis, MO, USA) and graphite powder (particle size: $1.65\text{ }\mu\text{m}$; purity: 99%, Seung-Lim Carbon Metal, Ansan, Korea) were milled via a high-energy ball mill (Pulverisette 7, Fritsch, Idar-Oberstein, Germany). In the milling process, WC–Co coated stainless steel jars and WC–Co balls with a diameter of 5 mm were used to minimize contamination. The ball-to-powder weight ratio (BPR) was 40:1. The carbothermal reduction was performed in a graphite vacuum furnace in vacuum (10^{-3} torr). Three kinds of heating rates of 5, 10 and 20 K min^{-1} were chosen and the heating was conducted in the temperature range of 923–1473 K. In order to characterize the variation of the phase constitutions with temperature during carbothermal reduction, the heating was stopped immediately when it reached to a specific temperature. The furnace cooling rate was higher than 100 K/min in the initial stage of cooling and it decreased slowly.

2.2. Characterization

Thermogravimetric analysis (TGA) and differential scanning calorimetry (DSC) were carried out using a TGA/DSCC at a heating rate of 10 K min^{-1} under a steady Ar flow of 200 ml. Samples were heated in the TGA/DSC to a target temperature of 1673 K, and then cooled down to room temperature under Ar flow.

X-ray diffraction (XRD) was performed on a D8–Advance X-ray diffractometer (Bruker, Billerica, MA, USA) with monochromatized Cu–K α radiation source ($\lambda=1.54056\text{ \AA}$) and using the Bragg-Brentano ($\Theta/2\Theta$) geometry. All samples were scanned in the range 20–120 with a 0.02° step size and $10^\circ/\text{min}$ scan speed.

The microstructure of the samples was characterized by field emission scanning electron microscopy (FESEM; MERLIN Compact, ZEISS, Oberkochen, Germany) and transmission electron microscopy (TEM; F20 FEI Tecnai, FEI, Hillsboro, OR, USA) operated at 200 KV. The carbide sizes of the samples were measured by line intercept methods using FESEM images.

III. Result and discussion

3.1. Reactions of $\text{WO}_3\text{-C}$ mixture during carbothermal reduction

The formation mechanism of WC nanopowder from $\text{WO}_3\text{-C}$ powder mixture was investigated using TGA/DSC, XRD, thermodynamic calculation and TEM analysis. Figure 1 shows TGA (black curve)/DSC (red curve) measurement results for $\text{WO}_3\text{-C}$ powder mixture. At a temperature range between 923 and 1238 K, a strong mass reduction was observed according to TGA (black curve), while no further mass losses were observed above 1190 K. This mass loss at the temperature range is believed to be the reduction reactions involving CO_2/CO gas evolution.

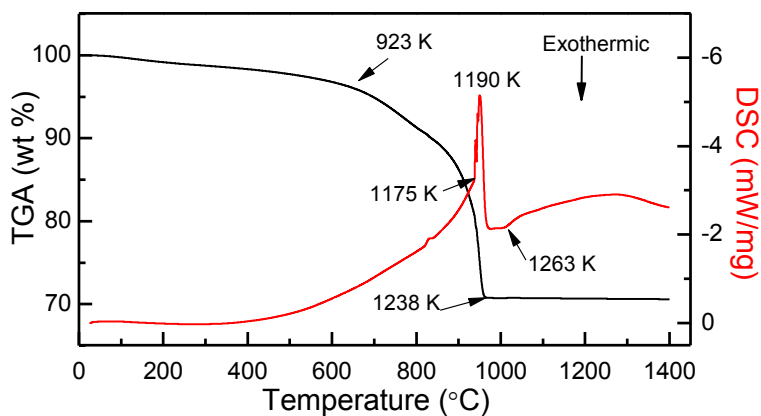


Figure 1. TGA/DSC curves for $\text{WO}_3\text{-C}$ mixture milled for 30 h. The black line indicates the TGA curve and the red line shows DSC curve.

According to DSC heat flow curve (red line), the sharp endothermic peak at 1190 K with a broad shoulder between 923 and 1175 K was detected, indicating that the reactions with a relatively small mass loss occurs gradually between 923 and 1175 K and fast reactions with a large mass loss occurs between 1175 and 1238 K. In addition, a broad endothermic peak without any mass loss between 1263 and 1400 K was observed, which is believed to be the carburization reactions by carbon.

In order to investigate the reactions associated with the features in the TGA/DSC curves, XRD measurement for the powder samples prepared by heating to specific temperatures at a heating rate of 10 K/min and subsequent cooling to room temperature were performed. The XRD patterns of the powder samples from the temperatures of 923, 1023, 1103, 1153 and 1373 K, which are before and after each reaction step, are shown in Figure 2. According to the resulting XRD patterns in Figure 2, the reduction and carburization of $\text{WO}_3\text{-C}$ mixture followed the sequential route of $\text{WO}_3 \rightarrow \text{WO}_{2.9} \rightarrow \text{WO}_2 \rightarrow \text{W} \rightarrow \text{W}_2\text{C} \rightarrow \text{WC}$, which is similar to previous work[32]. As-milled powder contained $\text{WO}_{2.9}$ and WO_2 phases, indicating that the raw WO_3 was partially reduced by mechanical activation and temperature rise during high energy ball milling.

The reaction step of $\text{WO}_{2.9} \rightarrow \text{WO}_2$ occurs very slowly from 673 K to 923 K and the phases present in the samples at 923 K are still $\text{WO}_{2.9}$ and WO_2 as shown in Figure 2. In the sample from 1023 K, only WO_2 phase was detected, indicating that $\text{WO}_{2.9}$ phase was completely reduced to WO_2 between 923 and

1023 K. These results reveal that the major reaction of $\text{WO}_{2.9} \rightarrow \text{WO}_2$ occurs between 923 and 1023 K. The reactions of $\text{WO}_2 \rightarrow \text{W} \rightarrow \text{W}_2\text{C}$ were rapidly proceeded and all phases were carburized to W_2C up to 1153 K, which corresponds to the strong mass loss on TGA curve, i.e. the sharp endothermic peak on DSC curve. Whereas, the reaction step of $\text{W}_2\text{C} \rightarrow \text{WC}$ occurs relative slowly and finished at 1373 K. Therefore, the broad endothermic peak on DSC curve between 1263 and 1400 K corresponds to the carburization of W_2C to WC, in which no remarkable mass losses were detected.

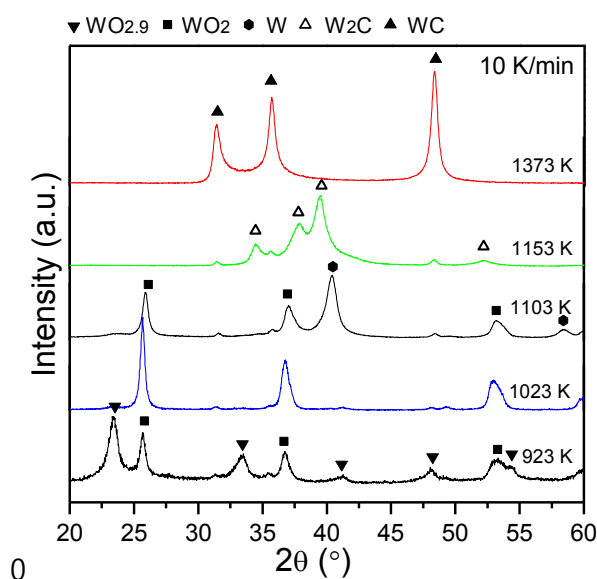
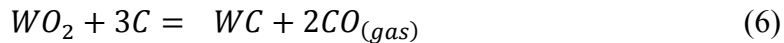
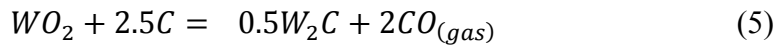
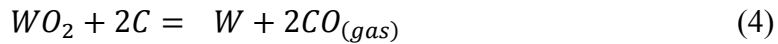
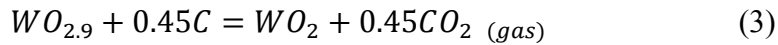
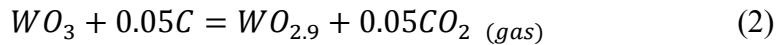
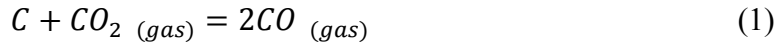


Figure 2. XRD patterns of $\text{WO}_3\text{-C}$ mixture at different temperatures during carbothermal reduction.

In order to investigate the tendency of the reactions during carbothermal reduction, the change of Gibbs free energy with temperature, ΔG_T , for possible reactions during the carbothermal reduction process were estimated, which determines the direction of the chemical reactions. The possible reactions can be expressed as follows;



The reaction according to Eq. (1) has a negative Gibbs free energy below 978 K, indicating that CO_2 and CO gas are stable below and above the temperature, respectively. Therefore, it is considered that below 978 K, the reactions involve CO_2 gas as a byproduct, while the reactions involve CO gas above 978 K.

The variation of ΔG_T for the above reactions are presented in Figure 3. The reactions according to Eq. (2) and (3), which occurs during high energy ball milling, have a negative ΔG_T value above 392 K (pink line in Figure 3a)

and 777 K (blue line in Figure 3a), respectively. The result demonstrates that the reactions could occur during high energy ball milling because the severe friction during milling is known to increase the temperature inside milling vessels up to 773 K. The reactions for Eq. (3) proceeded during early stage of the carbothermal reduction process up to 1023 K according to XRD results in Figure 1.

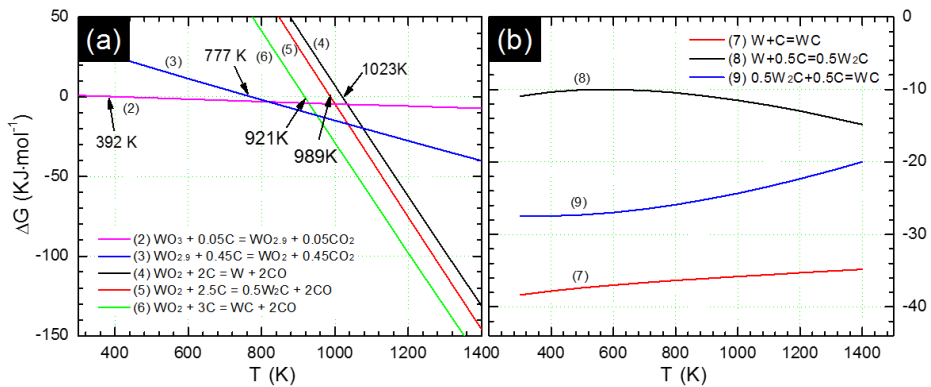


Figure 3. The variation of Gibbs free energy with temperature for the reactions during carbothermal reduction process of WO_3 -C mixture.

The reactions according to Eqs. (4), (5) and (6) have negative Gibbs free energies above 921 K, 989 K and 1023 K, respectively (see the black, red and green lines in Figure 3a). The ΔG_T values for Eqs. (4)-(6) have a much more negative than that for Eq. (3), which seem to enable the fast reaction between 1023 and 1153 K as shown in XRD patterns of Figure 2. In addition, the ΔG_T value for Eq. (6) is always more negative than those for Eq. (4) and (5), indicating that the reaction according to Eq. (6) is thermodynamically most probable. However, the actual reactions passed through the less probable path

of $\text{WO}_2 \rightarrow \text{W} \rightarrow \text{W}_2\text{C} \rightarrow \text{WC}$ as shown in Figure 2. According the results of thermodynamic calculation in Figure 3, the reaction for Eq. (4) can occur from 1023 K based on the results of thermodynamic calculation, but the reaction was already finished at 1023 K as shown in Figure 2. Kim et al.[32] reported previously that the reduction of carburization temperature and time might be due to the generation of many defects inside crystal structure of reactants.

For the carburization step of W into WC, the reactions according to Eqs. (7)-(9) have always a negative Gibbs free energy from room temperature to 1400 K as shown in Figure 3b. According to the variation of ΔG_T values in Figure 3b, the direct carburization of $\text{W} \rightarrow \text{WC}$ by carbon is most probable because the reaction for Eq. (7) has the lowest Gibbs free energy values at the temperature range concerned. However, the XRD results showed that the carburization of W followed the less probable route of $\text{W} \rightarrow \text{W}_2\text{C} \rightarrow \text{WC}$ as presented in Figure 2. These results imply that the reactions seem to be limited by the diffusion of certain elements.

In order to investigate whether the diffusion-controlled reactions or not, the phase evolution of $\text{WO}_3\text{-C}$ mixture with temperature was characterized at various heating rates. XRD patterns of $\text{WO}_3\text{-C}$ mixtures heated at two representative heating rates are shown in Figure 4. Comparing Figure 4 with Figure 2, each reaction step was delayed with increasing or decreasing the heating rate. The XRD patterns for the samples heated at a heating rate of 20 K/min are displayed in Figure 4a. $\text{WO}_{2.9}$ and WO_2 phases were detected at 1023

K, indicating that the reduction of $\text{WO}_{2.9} \rightarrow \text{WO}_2$ was not completed at the temperature. At 1153 K, the reaction of $\text{WO}_2 \rightarrow \text{W}$ was still in progress and the reaction of $\text{W}_2\text{C} \rightarrow \text{WC}$ was not completed at 1373 K. The delay of the reactions could be resulted from the lack of time for the reactions due to fast heating rate.

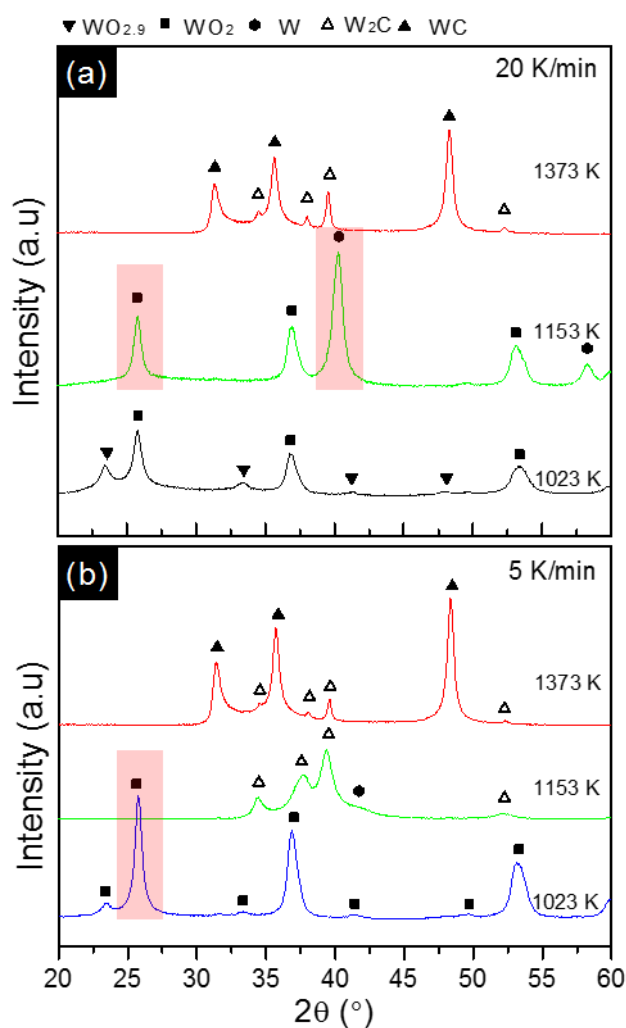


Figure 4. XRD patterns of WO_3 -C mixture with temperature and heating rate. (a) 20 K/min, (b) 5 K/min.

At a heating rate of 5 K/min, each reaction step was also delayed even though the time for reactions would be enough due to slow heating rate. Small amounts of residual $\text{WO}_{2.9}$, W and W_2C were detected at 1023, 1153 and 1373 K, respectively, indicating that the reactions were not completed.

One observation to note regarding the phase evolution during carbothermal reduction is the sharpness of XRD peaks of the intermediates. The peaks of W from 1153 K in Figure 4a, which is marked by a transparent red box, are more sharp than those from 1023 K in Figure 1, revealing that W particles grew because XRD peak broadness is related to the crystallite size. This implies that the growth of W particles is more dominant than the carburization reaction of W in the temperature range when heating rate is 20 K/min. The peaks of WO_2 from 1023 K in Figure 4b (transparent red box) are also more sharp than those of WO_2 from 1023 K in Figure 1. In this case, it is because WO_2 particles grow by a long dwell time in the temperature range due to slow heating rate, while there is no considerable reaction. These results reveal that the reason for the delay of the reactions is the growth of intermediates. The phase evolutions of $\text{WO}_3\text{--C}$ mixture with temperature and heating rate during carbothermal reduction are summarized in Table 3.

Table 2. The phase constitutions and their XRD peak sharpness of $\text{WO}_3\text{-C}$ mixture with temperature and heating rate.

Temperature (K)	5 °C/min			10 °C/min			20 °C/min		
	Constituents	Dominant Phase	Peak Sharpness	Constituents	Dominant Phase	Peak Sharpness	Constituents	Dominant Phase	Peak Sharpness
923	$\text{WO}_{2.9}$, WO_2	WO_2	Medium	$\text{WO}_{2.9}$, WO_2	$\text{WO}_{2.9}$	Medium	-	-	-
1023	$\text{WO}_{2.9}$, WO_2	WO_2	Sharp	WO_2	WO_2	Medium	$\text{WO}_{2.9}$, WO_2	WO_2	medium
1103	-	-	-	WO_2 , W	W	Medium	-	-	-
1153	W_2C , W	W_2C	Broad	W_2C , WC	W_2C	Broad	WO_2 , W	W	Sharp
1373	W_2C , WC	WC	Medium	WC	WC	Broad	W_2C , WC	WC	Medium

Figure 5 shows FESEM micrographs and grain size distributions of as-milled WO_3 -C mixture, the sample heated to 1373 K at a heating rate of 10 K/min and the sample heated to 1473 K at a heating rate of 20 K/min. WO_3 grains in as-milled WO_3 -C mixture were surrounded by carbon (the light grey particles in BSE-SEM image in Figure 5a). The as-milled powder has a very narrow grain size distribution and a small average grain size of 8.31 nm as shown in Figure 5d. Figure 5b shows FESEM image of the sample heated to 1373 K at a heating rate of 10 K/min. A comparison of Figure 5a and Figure 5b reveals that the morphology of WC powder heated at a rate of 10 K/min closely resembles that of the as-milled WO_3 -C mixture. The WC sample also has a narrow grain size distribution and small average grain size of 19.61 nm (Figure 5d). These results imply that WO_3 particles converted into WC without a notable shape change and growth during carbothermal reduction.

However, the sample heated to 1473 K at a rate of 20 K/min was partially sintered as shown in Figure 5c and has a broad grain size distribution and large average size of 47.30 nm (Figure 5d). Abnormally large grains (AG) were often observed as marked by arrows in Figure 5d, which are very detrimental for the sintering of nanostructured WC-Co bulk (ref to Section 2.3.2). The sample heated at a rate of 5 K/min has a similar morphology to the sample in Figure 5c. These results imply that the morphology and size of the product powder after carbothermal reduction are determined by the characteristics of initial WO_3 -C mixture and the conditions of carbothermal reduction process.

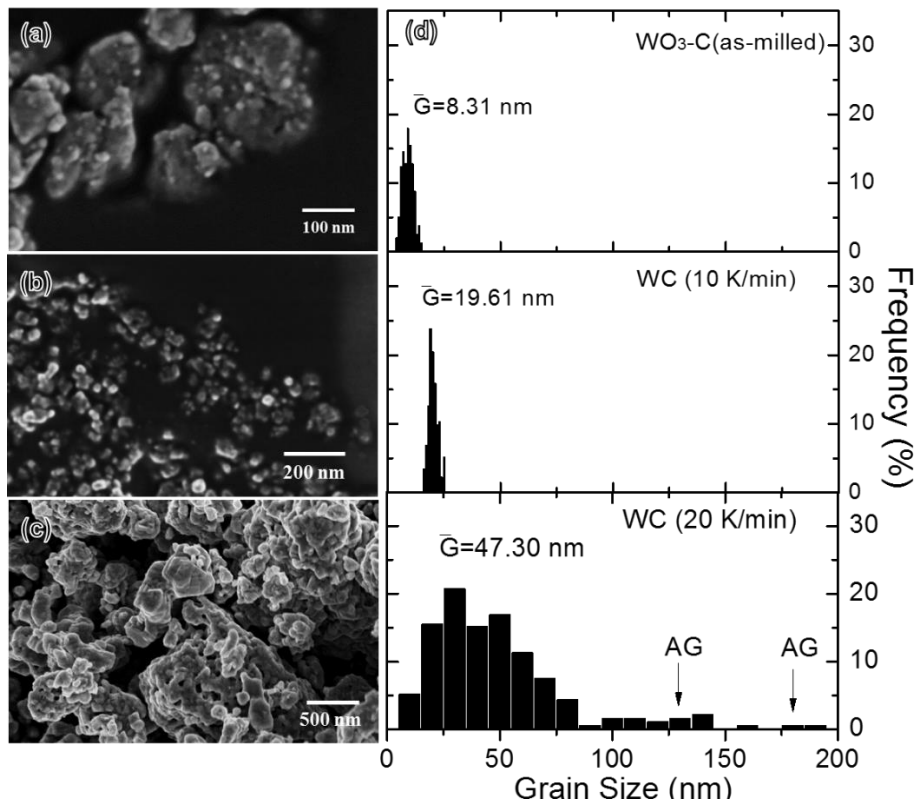


Figure 5. (a-c) FESEM micrographs of as-milled $\text{WO}_3\text{-C}$ mixture (a), the sample heated to 1373 K at 10 K/min (b) and the sample heated to 1473 K at 20 K/min (c). (d) The measured grain size distributions for the samples.

The microstructural evolution of the samples heated to 1273 K for 10 and 60 min were characterized using TEM analysis. The resulting HRTEM images are displayed in Figure 6. The sample heated to 1273 K for 10 min contains WC and W₂C particles as shown in Figure 6a. Most of WC particles are small in size, while W₂C particles are large in size. These results imply that the smaller the size of particles, the faster the reactions. Figure 6b shows the core/shell structure of particle from the sample heated to 1273 K for 30 min. It was identified that the core and shell correspond to W₂C and WC, respectively. The result reveals that the reaction of W₂C→WC is proceeded by forming of WC shell and growing of WC shell inward the core of particle. It will be controlled by the inward diffusion of carbon from the surface into the core of W₂C. Many papers[33-36] reported that the carburization of tungsten is controlled by the diffusion of carbon into tungsten particles or wires.

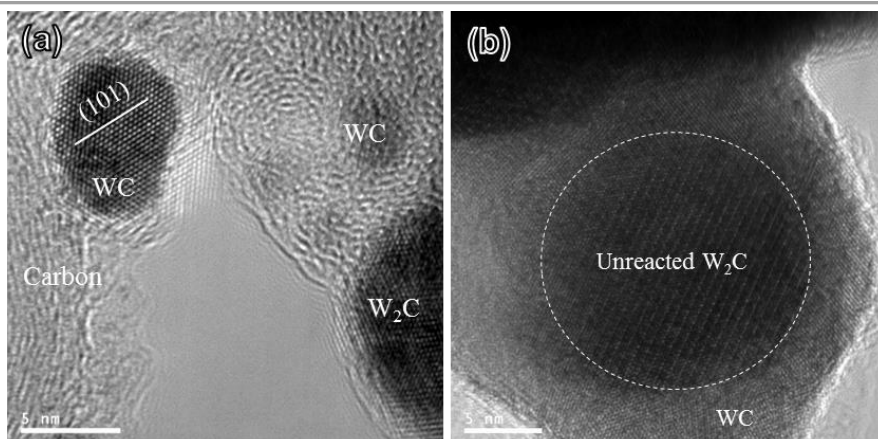


Figure 6. HR-TEM micrographs of WO_3 -C mixtures heated to 1273 K for two different holding times. (a) for 10 min and (b) for 60 min.

Based on these results, it can be supposed that the reduction of WO_3 is controlled by outward diffusion of oxygen and the carburization of W is controlled by inward diffusion of carbon. Considering the morphology of WO_3 -C mixture, the reduction and carburization process of WO_3 is schematically illustrated in Figure 7.

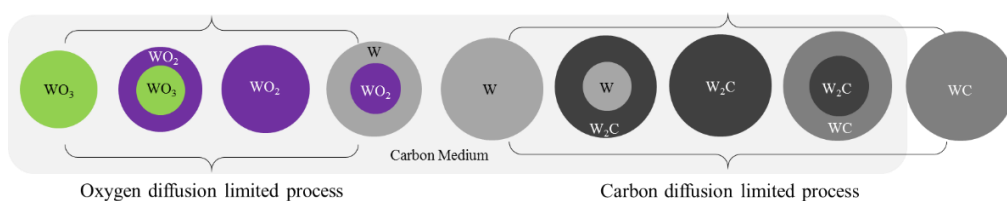


Figure 7. Schematic illustration of the reduction and carburization of WO_3 particles by carbon.

The supposition is verified using the carburization step of $W_2C \rightarrow WC$ as a model system. The model assumes a steady-state diffusion process across a growing shell of WC on spherical W_2C particle as illustrated in Figure 8, which is similar model as reported by Pirani and Sandor [37]. In this model, R is an initial radius of W_2C ball, which has been partially carburized into WC, and r is a residual core of W_2C . We assume that C_R is the carbon concentration at the particle surface, and C_r is the carbon concentration at the interface between growing the WC shell and the residual core of W_2C .

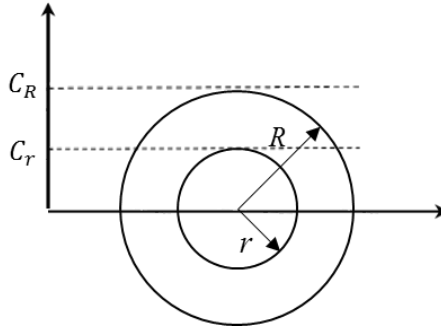


Figure 8. Schematic illustration of the spherical diffusion model in a steady-state.

The mathematical expression of this model becomes

$$\frac{d}{dr} \left(r^2 \frac{dC}{dr} \right) = 0 \quad (10)$$

The general solution of which is

$$r^2 \frac{dC}{dr} = -A \rightarrow C(r) = \frac{A}{r} + B$$

where the constants A and B could be determined from the specific boundary

conditions.

The flux of carbon through the WC shell, $J(r)$, is expressed as;

$$J(r) = -D \frac{dC}{dr} \quad (11)$$

Substituting the solution of Eq. (10) for Eq. (11), Eq. (11) becomes;

$$J(r) = D \frac{A}{r^2}$$

According to the model in Figure 8, the concentration at $r = R$ is C_R and the concentration at $r = r$ is C_r , which are unknown but are assumed to remain constant throughout the carburization. Then, the total flux of carbon through the WC shell can be reorganized as;

$$4\pi r^2 J(r) = -4\pi r^2 D \frac{dC}{dr} = 4\pi D \frac{(C_R - C_r)}{\left(\frac{1}{R} - \frac{1}{r}\right)}$$

where D denotes the diffusion coefficient of carbon through WC shell.

Therefore, the rate of penetration of carbon is given by following relation;

$$4\pi r^2 C_0 \frac{dr}{dt} = 4\pi D \frac{(C_R - C_r)}{\left(\frac{1}{R} - \frac{1}{r}\right)} \quad (12)$$

where t is the time and C_0 is the amount of carbon required to convert unit volume of W_2C into WC, $C_0 = C_{WC} - C_{W_2C}$. The integral of the Eq. (12) is written in the form

$$\int_R^r r^2 \left(\frac{1}{R} - \frac{1}{r}\right) dr = \int_0^t K dt$$

$$\int_R^r r^2 \left(\frac{1}{R} - \frac{1}{r}\right) dr = Kt \quad (13)$$

$$K = D \frac{C_R - C_r}{C_0} \quad (14)$$

and substituting r/R with x and integrating the right-hand side of Eq. (13), Eq. (13) can be rewritten as;

$$Kt = \left(\frac{R^2}{6}\right) \left[1 - 3\left(\frac{r}{R}\right)^2 + 2\left(\frac{r}{R}\right)^3\right] \quad (14)$$

where the cube of r/R is proportional to the weight fraction of residual W_2C .

The reaction rate and the end of the reaction step of $W_2C \rightarrow WC$ were theoretically estimated using Eq. (14) as a function of time at two different temperatures and for two different grain sizes of W_2C . For a comparison of the theoretical estimation and the experimental results, two temperatures of 1100 and 1200 °C, which are the temperatures for the completion of the reactions at heating rates of 10 and 20 K/min, respectively, were chosen. For a diffusion-controlled reaction, the completion of the reaction is determined by the largest grain in powder materials. Two grain sizes of 20 nm and 180 nm were chosen as the initial W_2C grain sizes, which approximately equal to the sizes of the largest grains at a heating rate of 10 and 20 K/min, respectively (ref. to Figure 5d). The reaction constant, K , in Eq. (14) was as a following relation, which taken from McCarty's work of the diffusion experiment using W powders[35].

$$K = 1.02 \times 10^{-8} \exp\left(-\frac{29300}{T}\right) m^2/s$$

The estimated values for $(r/R)^3$ using the conditions mentioned above are presented in Figure 9. The time for $(r/R)^3 = 0$ indicates the end of the carburization reaction for $W_2C \rightarrow WC$. For $R = 20$ nm, the reaction of

$W_2C \rightarrow WC$ was completed within a very short moment of 0.2 min at 1100 °C (blue curve in Figure 9), while for large initial size of $R = 180$ nm, the reaction was much delayed as long as 16.4 min at the temperature (black curve in Figure 9). When the reaction temperature increases to 1200 °C, the reaction time decreased by one forth (4.8 min) for the large size of $R = 180$ nm (red curve in Figure 9). These results are well consistent with the experimental results presented in Figure 2, 4 and 5, revealing that the carbothermal reduction reactions of WO_3 -C mixture are indeed diffusion-controlled reaction. The results reveal also that the time and temperature for the completion of the diffusion-controlled reaction decrease substantially with decreasing the grain size of reactant powder.

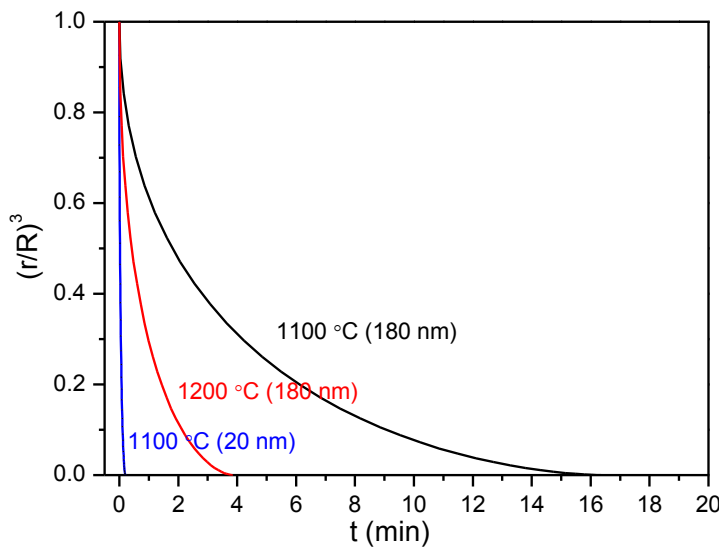


Figure 9. The variation of $(r/R)^3$ with time, temperature and the size of W_2C grain, R .

3.2. Grain growth of intermediates during carbothermal reduction

According to Figure 4 and 5, the clue for the grain growth of reactant and product powders during carbothermal reduction process was observed. In order to investigate the grain growth behavior during carbothermal reduction, the variation of WC grain size as a function of time was measured at two different temperatures of 1100 and 1200 °C as shown in Figure 10. The average grain sizes at 1200 °C (red circles) were always much larger than those at 1100 °C (black circles). The growth rate of WC grains at 1100 °C decreased early with time compared with that at 1200 °C.

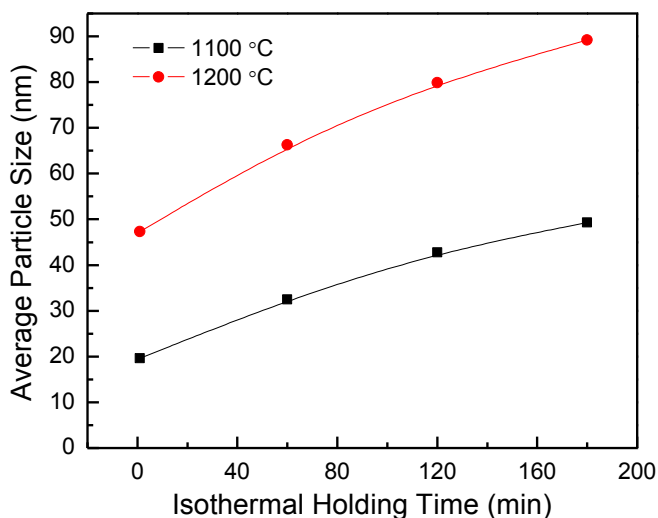


Figure 10. The variation of the average grain size of WC as a function of time at 1100 and 1200 °C.

The average grain sizes in Figure 10 are well fitted by the following relation;

$$\bar{a}_t^3 - \bar{a}_0^3 = K \cdot t \quad (15)$$

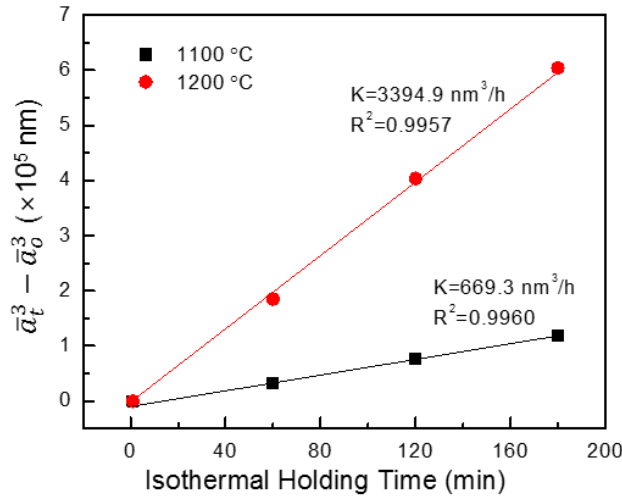


Figure 11. The variation in the cube of the average grain size of WC powder with holding time (t) at 1100 and 1200 °C, respectively.

The fitting results are shown in Figure 11. The values of least square of the linear regression (R^2) between $\bar{a}_t^3 - \bar{a}_0^3$ and time (t) were 0.9960 and 0.9957 for the samples at 1100 and 1200 °C, respectively, revealing a good linear relationship between $\bar{a}_t^3 - \bar{a}_0^3$ and t . This means that the growth of WC grains is proportional to $t^{1/3}$. In addition, the growth rate constant at 1200 °C (3394.9 nm³/h) is much larger than that at 1100 °C (669.3 nm³/h), revealing that the carbothermal reduction at high temperature is unfavorable for the synthesis of nano powders.

The important clues revealing the grain growth aspects of WC were

observed as shown in Figure 12. Figure 12 shows FESEM and TEM micrographs for the WC powder sample heated to 1473 K at heating rates of 20 K/min. In Figure 12a, the WC particles were severely agglomerated and partially sintered by forming the necks at the contact of grains. BF-TEM image in Figure 12b shows the enclosed morphology revealing the neck formation at the contact region of the grains mark by white dashed line. These results imply that the grain growth during carbothermal reduction process occurs in a manner similar to the shrinkage and growth during solid state sintering.

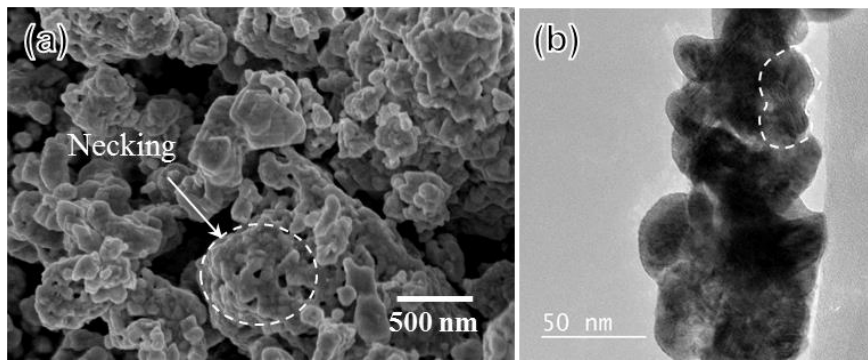


Figure 12. FESEM (a) and TEM (b) micrographs for the WC powder sample heated to 1473 K at a heating rate of 20 K/min.

Based on the experimental observations above, the grain growth behavior was theoretically modeled in order to investigate the influential factors for the grain growth of powders. Figure 13 shows two particle model describing the neck formation at the interface of two spherical grains suggested by Coble et al.[38].

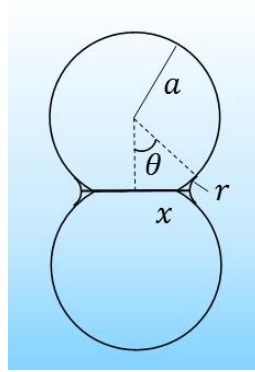


Figure 13. Two particle model for the formation of neck involving shrinkage during carbothermal reduction reaction.

In the model, the radius of curvature (r), area (A) and volume (V) of the neck between the particles with same radius of a can be described as follows;

$$r \approx \frac{x^2}{4a} \quad (16)$$

$$A \approx \frac{\pi x^3}{a} \quad (17)$$

$$V \approx \frac{\pi x^2 \cdot 2r}{2} = \frac{\pi x^4}{4a} \quad (18)$$

where x is the radius of the neck. These equations are derived considering the shrinkage which is taking account into closing the distance between particles when the neck grows. Here, the driving force is the difference

at the pressure, solubility and vapor pressure coming from the difference at the curvature radius of surfaces.

The paths for the material transfer in the system which can attribute to the growth of neck are schematically illustrated in Figure 14[39]. In the figure, the surface diffusion from the particle surface, the lattice diffusion from the particle surface, the grain boundary diffusion from the grain boundary, the lattice diffusion from grain boundary, the diffusion by evaporation and condensation and viscos flow, which can contribute to the material transfer in this system, are denoted by the diffusion coefficients of D_s , D_l , D_b , D_l , D_g and viscos flow, respectively, along with their direction (see arrows).

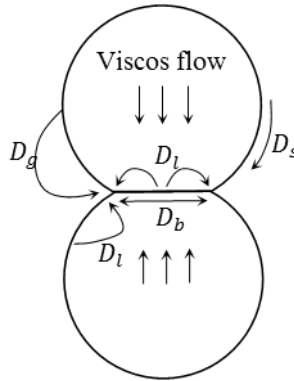


Figure 14. The schematic presentation of various diffusion paths contributed to the growth of neck.

Total growth rate of neck is determined by the summation of the growth rates of neck via six diffusion paths expressed as follows[39].

$$\left(\frac{dx}{dt}\right)_t = \sum_i^{i=6} \left(\frac{dx}{dt}\right)_i$$

It is reported that total growth rate of neck is governed by most dominant diffusion mechanism under given conditions. [40] In our system, the growth of

neck would be controlled by the surface diffusion from the particle surface to the neck because the carbothermal reduction is carried out at much lower temperatures than the melting temperature of the intermediates and the surface area is very high due to the small grain size. Therefore, the surface diffusion for the growth of neck is only considered hereinafter.

The surface diffusion from the particle surface to the surface of the neck is from the work of G. C. Kuczynski et al.[41]

$$\frac{dV}{dt} = JAV_m \quad (19)$$

$$\frac{dV}{dt} = \frac{2\pi x^3}{a} \frac{dx}{dt} = \frac{D_s}{RT} \nabla \sigma \cdot A \cdot V_m = \frac{D_s}{RT} \left(\frac{\gamma}{r} \cdot \frac{1}{r} \right) 2\pi x \cdot 2\delta_s V_m$$

$$x = \sqrt[7]{\frac{56D_s\delta_s\gamma V_m a^3}{RT} \cdot t} \quad (20)$$

where J is the flux, t the time, V_m the molar volume, D_s the surface diffusivity, $\nabla \sigma$ the gradient of stress, R the gas constant, T the absolute temperature, γ the surface energy and δ_s the thickness of surface diffusion layer.

During carbothermal reduction, the grain growth occurs simultaneously with the formation of neck. Thus, the grain growth was modeled considering the neck formation as illustrated in Figure 15. For the sake of simplicity, the material transfers at the interface of two grains was modeled and extended to a multi-dimensional system. Assuming that two spherical grains with a different radius have a neck at their interface, the surface diffusion and the diffusion perpendicular to the grain boundary are possible paths for material transfers as illustrated in Figure 15.

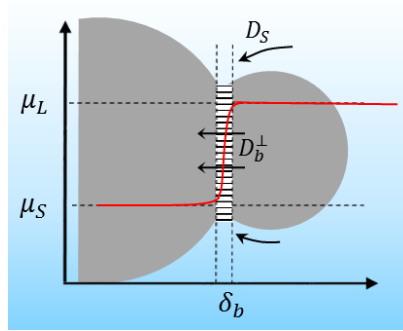


Figure 15. Schematic presentation of the grain growth during carbothermal reduction through the diffusion of surface and the diffusion perpendicular to the grain boundary.

In a real system, the boundaries at the interfaces of grains have a curved shape depending on surrounding grains and their interfacial energy. Therefore, the grains on either side of their interface undergo a different stress. If the atoms belonging to the grains are in local equilibrium and the curvature radius is R_o , the difference in stress is $\Delta\sigma = 2\gamma/R_o$. Then, the volume change of grains with time can be expressed as a same formula of Eq (19). In Eq. (19), A indicates the total area of the grain boundary. In the powder materials, one grain has many contacts with several other grains in powder agglomerates. Therefore, the total area becomes a simple summation of the areas of each boundary as follows.

$$A = \sum_{i=1}^n A_i$$

where A_i is the grain boundary area of each grain.

When the grain growth occurs via the diffusion with the direction perpendicular to the grain boundary, the area of each grain boundary can be expressed as $A_i = \pi x_i^2$. Then, total contact area of grain boundary can be

approximated as follows.

$$A \approx n\pi\bar{x}^2 \quad (21)$$

where n is the coordination number which describes the average number of the contacts of the grains in powder agglomerates. Then, the increase rate of an average grain size can be expressed as follows.

$$4\pi\bar{a}^2 \frac{d\bar{a}}{dt} = \frac{D_b^\perp}{RT} (\nabla\sigma) \cdot n\pi\bar{x}^2 \cdot V_m$$

where D_b^\perp is the diffusivity from grain boundary to the direction perpendicular to the boundary and $\nabla\sigma$ the gradient of stress which is $\nabla\sigma = \Delta P \cdot 1/L$. Here, assuming that the stress is working through the grain boundary, L becomes equal to the grain boundary thickness, δ_b .

$$\frac{d\bar{a}}{dt} = \frac{D_b^\perp}{4\bar{a}^2 RT} \frac{2\gamma V_m}{R_o \delta_b} n\bar{x}^2 \quad (22)$$

Because the curvature radius of grain boundary is simply proportional to the average grain size, the above relation can be rewritten as follows.

$$\frac{d\bar{a}}{dt} = \frac{\alpha n D_b^\perp \gamma V_m}{2RT \delta_b \bar{a}^3} \bar{x}^2 \quad (23)$$

where α is the proportional constant. Substituting Eq. (20) for x in Eq. (23), we can get the relation for the grain growth by the diffusion with the direction perpendicular to the grain boundary as follows.

$$\bar{a}_t^5 - \bar{a}_o^5 = 9.6 \cdot \alpha^{\frac{7}{3}} \cdot n^{\frac{7}{3}} \cdot \left(\frac{D_b^\perp}{\delta_b}\right)^{\frac{7}{3}} \cdot \left(\frac{\gamma V_m}{RT}\right)^3 \cdot (D_s \delta_s)^{\frac{2}{3}} \cdot t^3 \quad (24)$$

According to Eq. (24), the average grain size is proportional to $t^{0.6}$. In addition, the average grain size can increase with increase in the coordination number ($\bar{a} \propto n^{0.47}$).

When the grain growth occurs through the surface diffusion, the volume change with time can also be represented by the Eq. (19). In this case, the area of surface diffusion at each contact can be determined as follows.

$$\begin{aligned} A_i &= \int_{x-\delta_s}^x 2\pi x dx \\ &= \pi x^2 - \pi(x - \delta_s)^2 = 2\pi x \delta_s - \pi \delta_s^2 \approx 2\pi x \delta_s \end{aligned} \quad (25)$$

where δ_s is the thickness of surface diffusion layer. Then, total area of surface diffusion becomes $A \approx n2\pi\bar{x}\delta_s$ similar to the diffusion perpendicular to the grain boundary.

The increase rate of an average grain size can then be expressed as:

$$\frac{d\bar{a}}{dt} = \frac{nD_s}{2\bar{a}2RT} (\nabla\sigma) \bar{x} \delta_s V_m$$

If the lengths affected by stress is about the thickness of boundary layer, δ_b , the gradient of stress can be expressed as the same term in Eq. (22). Then, above equation can be reorganized as:

$$\frac{d\bar{a}}{dt} = \frac{nD_s\delta_s V_m}{2RT\bar{a}2} \bar{x} \left(\frac{2\gamma}{\bar{R}\delta_b} \right) = \frac{nD_s\delta_s\gamma V_m}{RT\delta_b\bar{a}3} \bar{x} \quad (26)$$

where \bar{R} is the average curvature radius which is replaced by \bar{a} because the average curvature radius is the same with average grain size.

Similarly, substituting Eq. (19) for \bar{x} in Eq. (26), we can get the relation for the grain growth by surface diffusion as follows.

$$\bar{a}_t^{25} - \bar{a}_0^{25} = 56 \left(\frac{n}{\delta_b} \right)^7 \left(\frac{D_s\delta_s\gamma V_m}{RT} \right)^8 \cdot t^8 \quad (27)$$

According to the equation, when the growth occurs via the surface diffusion, the average grain size is proportional to $t^{0.32}$ and $n^{0.28}$.

According to the experimental results in Figure 11, the average grain size is approximately proportional to $t^{0.33}$, which is more closer to the relation of Eq. (27) rather than that of Eq. (24). These results indicate that the growth of WC grains during carbothermal reduction is mainly governed by the surface diffusion. In this work, the surface area of WC nanopowder would be very high due to the extremely small grain size as small as 10 nm. The growth rate is proportional to the area of surface diffusion, which is not simply related to the surface area of WC grains, but is depending on the area of the neck according to Eqs. (25) and (26). In addition, the close contact between grains is detrimental for the synthesis of nanopowder because the diffusion area increases with the coordination number, n .

3.3. Synthesis of Nanopowders via grain growth controlled method.

The results founded by the systematic experiments and theoretical approaches above were applied for the synthesis of nanopowders. Figure 16 shows FESEM images for the several carbide and metal nanopowders synthesized via the grain growth controlled method. Figure 16 a, b, c, d, e and f show the WC, VC, TiC, $(\text{Ti}_{0.88}\text{W}_{0.12})\text{C}$, Co and Ni nanopowders, respectively, which are about 10, 30, 50, 30, 20 and 20 nm in average grain size, respectively.

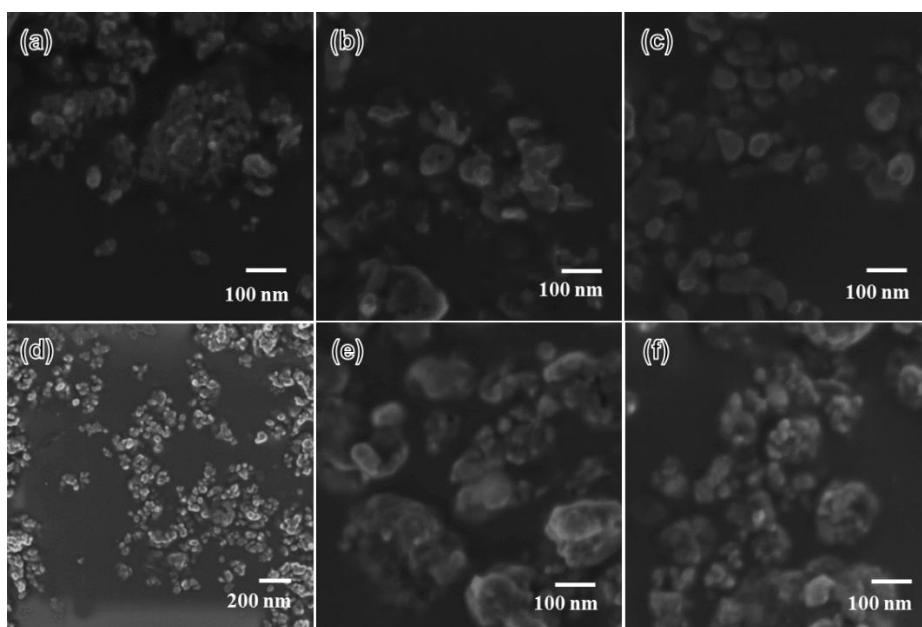


Figure 16. FESEM images for the nanopowders synthesized via grain growth controlled method. (a) WC (10 nm), (b) VC (30 nm), (c) TiC (50 nm), (d) $(\text{Ti}_{0.88}\text{W}_{0.12})\text{C}$ (30 nm), (e) Co (20 nm), (f) Ni (20 nm).

According to the results in Section 2.3.1, all the reactions were completed during heating and the rate of the reactions was varied with heating rate. Therefore, the heating stage should be controlled in order to synthesize nanopowders. Based on experimental and theoretical analyses, the smaller the grain size, the faster the reaction rate. According to Figure 2 in Section 3.1.1, most of reactions was rapidly completed within a very short time once temperature reaches at a certain point. However, when the heating rate changed, the reactant grains grew during heating, which delays the carbothermal reduction and causes further grain growth.

According to Figure 1 in Section 3.1.1, the reactions in the temperature range from 400 to 1175 K occurs gradually, which is attributed to the slow diffusion kinetics of oxygen inside $\text{WO}_{2.9}$ and WO_2 grains. If the $\text{WO}_{2.9}$ and WO_2 grains are stayed at high temperature or underwent too high temperature, $\text{WO}_{2.9}$ and WO_2 grains will grow fast before reacted because the enough time for growth will be given, or the metastable intermediates become more unstable at high temperature. Therefore, the carbothermal reduction at the temperature range should be conducted by the gradual heating with an appropriate heating rate. The sharp peak in Figure 1 is corresponded to the reaction according to Eqs. (4) and (8), which are very fast reactions at the temperature range of 1175-1238 K. These fast reactions could be attributed to the small grain size of remaining WO_2 grains and the fast diffusivity of carbon inside W grains. Therefore, a fast heating rate would be better to be applied for the carbothermal reduction in the temperature range. Above 1263 K, the gradual reaction with a broad peak of DSC curve in Figure 1 is corresponding to the reaction of Eq. (9).

The slow reaction is attributed to the slow diffusion of carbon through the WC shell. Therefore, an appropriate time for carbon diffusion without growth should be given by adjusting heating rate.

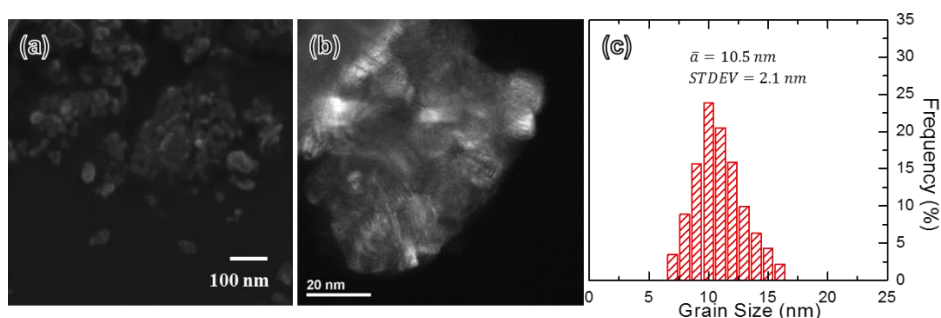


Figure 17. FESEM, DF-TEM images and the grain size distribution of WC nanopowder synthesized via the grain growth controlled method.

Figure 17 shows FESEM, DF-TEM micrographs and the grain size distribution of WC nanopowder synthesized via the grain growth controlled method. WC grains in the powder were well separated with each other, which means less agglomeration, and homogeneous in size as shown in FESEM and DF-TEM micrographs. The grain size distribution of WC nanopowder is narrow with an average grain size of 10.5 nm and standard deviation (STDEV) of 2.1 nm. Using this method developed in this study enables us to successively produce various nanopowders such as carbides, carbonitrides, and some metal powders.

IV. Conclusion

An experimental and theoretical analyses of the reactions and growth during carbothermal reduction were systematically made in a $\text{WO}_3\text{-C}$ mixture milled by high energy ball mill, and the new methodology for the fabrication of various nanopowders was developed. The main results can be summarized as follows:

1. The carbothermal reduction of $\text{WO}_3\text{-C}$ mixture is controlled by the outward diffusion reaction of oxygen and the inward diffusion reaction of carbon in spherical reactant grains. A theoretical estimation for the reactions during carbothermal reduction reveals that the smaller the grain size is, the faster the reactions are.
2. The experimental results for the growth of WC grains is fitted by linear regression between the cube of average grain size (\bar{a}^3) and time (t). A theoretical approach for the grain growth represents that the growth of WC grains is mainly controlled by the surface diffusion, and the average grain size is proportional to $\sim t^{0.32}$, which is well consistent with the experimental results. The grain growth rate increases with the coordination number, revealing that the loose packing of raw powder mixture during carbothermal reduction is beneficial for the fabrication of nanopowders.
3. WC nanopowder with an extremely small grain size of 10.5 nm was successfully synthesized by the grain growth controlled method.

Part II

Synthesis of Nano WC–Co Composites

I. Introduction

1.1. Mechanism of grain growth inhibition of WC during Liquid Phase Sintering

The addition of second elements has been used as an essential technique to oppose the grain growth in the powder metallurgical process for nanostructured materials design. Nanoscale carbide structure provides the materials with interesting properties such as high strength and wear resistance, but it is very difficult to obtain nanostructured materials due to a large driving force for growth. In a liquid phase sintering (LPS), especially, the growth of nano particles is more accelerated due to an enhanced material transfer through liquid phase. WC–Co (cemented carbide) composite is one of the typical examples with LPS.

Wang et al.[42] studied the carbide growth behavior of nano WC–Co powder during early stage of sintering. They reported that after heating to 1400 °C without a hold, the carbides of 10 nm in size initially increased to about a hundred times. Such an explosive growth of WC particles in Co phase could be significantly retarded with the small additions of the second phases such as VC and Cr_3C_2 during all stages of sintering–heating, holding and cooling stages. Wang et al. also reported that during heating, WC particles scarcely grew until 1300 °C with a small addition of VC, and the average particle size was one tenth smaller than pure WC–Co system after heating to 1400 °C.

During past two decades, many papers were devoted to reveal the mechanism of the carbide growth inhibition (CGI) due to such a sought-after

effect [43-58]. Hyoungh et al.[58] suggested that the particle growth inhibition of WC by VC addition is related to the increase in 2-dimensional nucleation (2-DN) barrier due to an increased edge energy. This explanation is based on the symptoms in a topological level—the change of thermodynamic equilibrium shape of WC particles from a truncated triangular prism to a triangular prism without a truncation by VC addition, which causes the increase in an edge energy. This shape transition may be a change of WC/Co interfacial character, but its underlying cause was not presented in the paper.

The first attempt to characterize the interfaces in an atomic level was conducted by Jaroenworarluck et al.[43]. They observed V segregation on two habit planes of WC, (0001) basal plane and $(10\bar{1}0)$ prismatic plane, which consist of WC surfaces. Since first reported by Jaroenworarluck et al., many papers have reported the V segregation on the WC particle surfaces[44-57]. However, there are several controversial reports from two different stances due to the difficulty for the observation of the interface structure at high temperatures. One side, Kawakami et al.[46-48] insisted that there was no V segregation during heating up and holding stages of LPS, and it just occurred during cooling stage. They suggested that V segregation itself is not directly correlated to the CGI effect, but the carbide growth is inhibited by the intermittent adsorption and desorption of V atoms on the WC surfaces during LPS.

The other side asserts that GGI of WC occurs by forming (V,W)C segregation layers on the WC surfaces during LPS. Sugiyama et al. [51, 53] examined the WC/Co interfaces for the quenched VC-doped WC-Co

specimens after sintered at 1380 °C for 1 h. In these studies, they tried to prove that (V,W)C segregation layers were existed at even LPS temperature. Johansson and Wahnstrom[50, 52] conducted theoretical studies for the stability of the thin (V,W)C cubic layers in WC/Co interfaces. They reported that (V,W)C segregation layers could be stable at least on (0001) basal planes of the WC carbides at a wide range of LPS temperatures.


The current status of the discussion for GGI is thus in the stage to prove the existence of V segregation layers during holding stage of LPS. Although their works suggested that the (V,W)C segregation layers were stable during LPS, neither detailed exploration of the carbide growth behavior of VC-doped WC-Co system nor detailed role of the (V,W)C layers were addressed. Moreover, the fastest carbide growth of nanosized WC-Co occurs during heating stage, and it is effectively impeded by the VC addition[42, 59]. However, these works have not explicitly revealed the mechanism of the early stage consolidation-relevant carbide growth and action of the inhibitors.

1.2. Synthesis of nano WC-Co Composites via liquid phase sintering

To best of our knowledge, no studies for sintered WC–Co composites with a nanostructure (<50 nm) were reported up to now even though the main challenge of this field is to achieve the genuine nanostructured WC–Co. Table 2 shows the results from the literature related to the synthesis of the nanostructured WC–Co composites. Although high pressure assisted sintering or rapid sintering techniques such as hot isostatic pressing and spark plasma sintering, which are not feasible for the mass production, were employed to avoid a rapid grain growth during sintering, the nanostructured WC–Co composites with a grain size less than 50 nm were seldom reported.

Table 3. The summarization of the results related to the sintering of the nanostructured WC–Co composites from literature[1, 60].

Sintering Process	Process T and <i>t</i>	Pressure (MPa)	Heating rate (°C/min)	Powder grains size (nm)	Inhibitors	Relative density (%)	Sintered grain size (nm)	Ref.
Hot pressing	1300 °C, 20 min	30	N/A	-	0.6VC	100	169	[61]
Hot pressing	1700 °C, 43 Ks	1500	N/A	7	No	100	95	[31]
Hot pressing	1300 °C, 90 min	25	N/A	80	No	100	780	[62]
SPS ^a	1100 °C, 5 min	25	N/A	80	No	100	780	[62]
HIP ^b	1000 °C, 1 h	150	N/A	-	No	100	400	[63]
HIP	1000 °C, 1 h	150	N/A	-	0.4VC	100	200	[63]
SPS	1150 °C, 10 min	60	N/A	-	No	98	230	[64]
SPS	1100 °C, 10 min	60	150	40-250	No	99.89	800	[65]
SPS	1100 °C, 10 min	60	150	40-250	1VC	95.94	470	[65]
SPS	1240 °C, 2 min	60	100	50	No	-	280	[66]
SPS	1240 °C, 2 min	60	100	50	0.9VC	-	170	[66]
SPS	1150 °C, 5 min	10 KN	100	33	No	-	200	[67]
SPS	1200 °C, 5 min	30	N/A	11	0.8VC	95.1	<100	[68]
SPS	1000 °C, 10 min	100	100	100	No	-	350	[69]
HFIHS ^c	1200 °C, 55 s	60	1400	100	No	99.4	323	[70]



PPS ^d	1100 °C, 5 min	60	1000-1200	60	No	98	50	[71]
ROC ^e	1000 °C, 10 s	830	N/A	-	No	94.6	150	[72]
UPRC ^f	1200 °C, 15 min	1000	200	50	No	99.4	97	[73]
SPS	1100 °C, 5 min	50	200	75 (10 x-tallite)	2VC	100	70	[60]

^a Spark plasma sintering

^b Hot isostatic pressing

^c High frequency induction-heated sintering

^d Pulse plasma sintering

^e Rapid omni compaction

^f ultrahigh pressure rapid hot consolidation

1.3. Purpose of the work

In this part, we demonstrated the possibility for the synthesis of genuine nanostructured WC–Co composites via liquid phase sintering for WC–Co composites with a thorough investigation for the underlying mechanisms of the grain growth inhibition during liquid phase sintering.

VC was exploited as a dopant opposing grain growth during liquid phase sintering. The present work focuses on the structural evolution of VC–doped WC–Co system with a nanostructure during the early stage of sintering through an atomic level analysis. We demonstrate the mechanism of grain growth inhibition by the formation of (V,W)C segregation layers and suggest a scalable pathway for genuine nanostructured WC–Co composites with < 50 nm carbide size. The system exhibited a very high stability of nanostructure for a long time-at-temperature up to relatively high temperatures and showed somewhat unusual microstructural characters.

II. Experimental procedure

2.1. Materials and methods

Tungsten trioxide powder (particle size: $\leq 20\ \mu\text{m}$; purity: 99%; Sigma-Aldrich, St. Louis, MO, USA) and graphite powder (particle size: $1.65\ \mu\text{m}$; purity: 99%, Seung-Lim Carbon Metal, Ansan, Korea) were milled via a high-energy ball mill (Pulverisette 7, Fritsch, Idar-Oberstein, Germany). In the milling process, WC–Co coated stainless steel jars and WC–Co balls with a diameter of 5 mm were used to minimize contamination. The ball-to-powder weight ratio (BPR) was 40:1. For the fabrication of WC nanopowder, the as-milled powder mixtures were heated up to $1100\ ^\circ\text{C}$ for carbothermal reduction and carburization at a heating rate of $10^\circ\text{C}/\text{min}$ under vacuum (10^{-3} torr) in a graphite vacuum furnace and kept for 10 min at the temperature, and furnace-cooled to room temperature.

Pure cobalt powder (particle size: $2.3\ \mu\text{m}$; purity: $>99\%$; Cobatech Co., Ansan, Korea) and mixture powder of Co and vanadium carbide (particle size: $\leq 20\ \mu\text{m}$; purity: 99%; Alfa Aesar) were milled separately by the high-energy ball mill to reduce grain size in an ethyl alcohol at 200 rpm for 20h. WC nanopowder was blended with the as-milled pure Co and Co–VC mixture powder to reach target compositions of WC–15 wt %Co and WC–14.5 wt %Co–1.5 wt %VC, respectively. The blending process was carried out in an ethyl alcohol media using WC–Co balls in plastic bottles. The BPR was 10:1, and the rotation was at 200 rpm for 20h. The mixed slurries were dried and then

sieved (125 mesh) to remove agglomerates. The powder mixtures were pressed into discs of 1 cm in dia. under a pressure of 150 MPa.

To characterize the carbide growth of pure and VC-doped WC–Co system, the green discs were sintered in a graphite vacuum furnace ($\sim 10^{-3}$ torr) in the temperature range of 1200–1350 °C for various durations.

For the characterization of interfaces, the green compacts were heated up to 1300 °C in a vacuum with a heating rate of 10 °C/min, and kept at the temperature for 10 min to homogenize the composition of V, and then cooled down to 1200 °C, and held for 1 h to reach the equilibrium composition and microstructure, and subsequently quenched into water vessel. Thin samples for transmission electron microscopy (TEM) observation were prepared from the specimens quenched at 1200 °C with focused ion beam (FIB) in a Helios 650 NanoLab instrument (FEI, USA) using 15 KeV Ga⁺ ions for initial thinning and 5 KeV Ga⁺ ions for final thinning.

2.2. Characterization

The prepared specimens were characterized by MERLIN Compact FESEM. The carbide sizes of the samples were measured by line intercept methods using back scattered electron (BSE) FESEM images.

Spherical aberration-corrected scanning transmission electron microscopy (Cs STEM) was performed using a JEM-ARM200F microscope (Cold Field Emission Type, JEOL, Japan) operated at 200 KV (HADDF detector: 8 cm, semi-angle of convergence: 68~280 mrad). Compositional distribution was investigated using energy dispersive X-ray spectroscopy (EDS) in STEM mode.

III. Result and Discussion

3.1. WC growth in undoped WC–Co

The resulting WC nanopowder was 19.5 nm in an average particle size with a standard deviation of 2.2 nm as measured by FESEM images.

For the characterization of pure WC–Co system, a fast heating rate (300 °C/min) was applied to minimize the growth of WC during heating stage. Figure 18 shows typical FESEM micrographs and particle size distributions exhibiting a fast WC growth during heating. Fig. 18a and 18b are from the samples sintered at 1250 °C and 1350 °C for 1 min, respectively. After sintering at 1250 °C for 1 min, a few very large WC particles are observed in the pool of the very small WC particles as shown in Fig. 18a. In contrast to those at 1250 °C, no small carbides are observed at 1350 °C as presented in Fig. 18b. Fig. 18c shows the measured 2-D carbide size distributions of the samples sintered for 1 and 10 min at two different temperatures along with the average carbide size. With increasing temperature and time, the particle size distribution was broadened and the average size of WC particles increased drastically. After 1 min at 1250 °C, only few numbers of WC particles grew greatly, while the remaining WC particles did not grow appreciably. After 10 min hold at the temperature, no small particles are observed. At 1350 °C, only large particles are observed from the early stage of 1 min hold, and the size of large particles became larger and the numbers of large particles increased consuming small particles with time. Considering these grain growth behavior, the fast growth rate of nano WC particles must be a result of abnormal growth.

Wang et al.[42] suggested that the fast carbide growth of nano WC carbides occurs by the coalescence between WC carbides. Although most of the large carbides at a high temperature can be explained in terms of coalescence, the faster growth rate of the largest carbide at a low temperature cannot be explained.

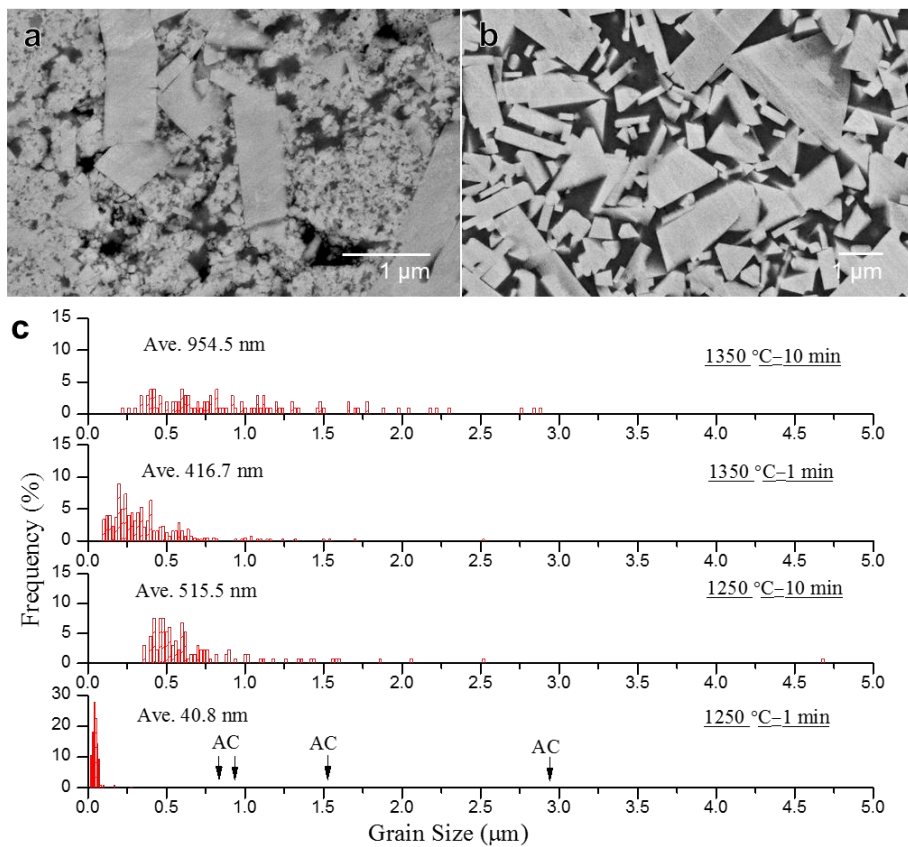


Figure 18. FESEM micrographs and grain size distribution for pure WC-Co samples sintered at two representative temperatures and times. A fast heating rate of 300 °C/min was employed in order to minimize the grain growth during heating: (a) 1250 °C for 1 min (b) 1350 °C for 1 min, (c) the particle size distribution along with the average size.

The observed microstructural evolution can be well explained by the mixed control model of the grain growth suggested by Kang et al.[74-82], which reflects the coupling effect of the maximum driving force for growth (Δg_{max}) and the critical driving force for appreciable migration of the interface (Δg_c) [78, 79]. According to their theory, the grain growth of the system with a faceted interface occurs in a manner of mixed-control expressed as follows[78].

$$v_M \equiv \frac{dr}{dt} = \left(\frac{1}{v_D} + \frac{1}{v_R} \right)^{-1} \quad (28)$$

where r is the radius of carbide, v_D the growth rate controlled by diffusion and v_R the growth rate controlled by interfacial reaction. For the growth kinetics by diffusion, Ardell's model[83] was used. v_D and v_R are then expressed as

$$v_D \equiv \frac{dr}{dt} = \frac{A}{r} \left(\frac{1}{r^*} - \frac{1}{r} \right) \cdot \left(1 + \beta(V) \frac{r}{r^*} \right) \quad (29)$$

$$v_R \equiv \frac{dr}{dt} = B \exp \left(- \frac{C}{\frac{1}{r^*} - \frac{1}{r}} \right) \quad (30)$$

Here, r^* is the critical radius of carbides neither growing nor shrinking and $\beta(V)$ the function of precipitate volume fraction (V). $A(= 2\gamma V_m D C_\infty / RT)$, $B(\propto h)$ and $C(= \pi \sigma^2 / 6kTh\gamma)$ are constants that depend on interfacial energy (γ), diffusion coefficient (D), the concentration of the saturated solution (C_∞), step height (h), step free energy (σ), and temperature (T).

According to Eqs. (28)–(30) above, there is a critical driving force for growth, Δg_c , due to 2-dimensional nucleation which depends mainly on the step free energy (σ) and temperature (T) as Eq. (31).

$$\Delta g_c = E \frac{\pi \sigma^2}{kTh} \quad (31)$$

where E is a constant, which is independent on σ , T and h . According to Eq. (4), Δg_c is proportional to the square of σ and inversely proportional to T . The carbides with a larger driving force than the Δg_c can selectively grow, resulted in abnormal grain growth (AGG).

The evolution of the abnormal carbides in Fig. 18 can be explained by means of the change of Δg_c . At low temperatures, only a few carbides can grow fast abnormally due to a large Δg_c . At high temperatures, more carbides can grow fast as Δg_c decreases with temperature. The driving force for the growth is determined by its size relative to the average carbide size[82], which is expressed as:

$$\Delta g = 4\gamma \left(\frac{1}{\bar{r}} - \frac{1}{r} \right) \quad (32)$$

if the mean field concept is accepted. Here, \bar{r} is the average carbide size. To approximate the driving force of the largest carbide, Δg_{LG} , the interfacial energy is assumed to be 0.1 J/m²[84] although it varies with temperature and the interfacial orientation relationship. Their driving forces is calculated based on the average carbide sizes and the largest carbide sizes presented in Fig. 18c. The estimated Δg_{LG} for the samples sintered at 1250 and 1350 °C for 1 and 10 min, respectively, are 9.8×10^6 J/m³, 7.0×10^5 J/m³, 8.0×10^5 J/m³ and 2.8×10^5 J/m³ in the same order of that in Fig. 18c.

The variation of Δg_{LG} with temperature and time, Δg_{LG}^{T-t} , and the variation of Δg_c with temperature, Δg_c^T , are schematically illustrated as a

function of growth rates and driving forces in Fig. 19. The growth rate of the carbides with the driving force larger than Δg_c increases with temperature due to the increased atom mobility. Nonetheless, the growth rate of the largest carbide at 1250 °C (the blue open circles in Fig. 19) is greater than that at 1350 °C (the red open circles) due to its large driving force, Δg_{LG}^{1250-t} .

Based on these results, we conclude that the carbide growth in WC–Co system occurs by mixed-control mode rather than the coalescence. The results imply that the nanostructure of WC–Co is extremely vulnerable to the carbide growth, which makes it difficult to obtain nanostructure by a traditional technique.

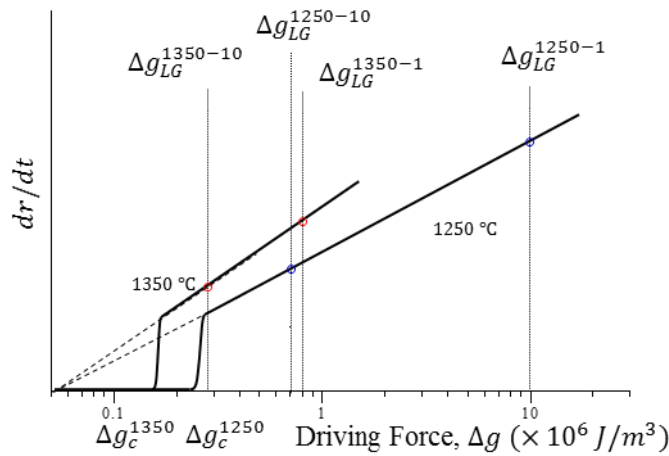


Figure 19. Schematic illustration of the critical driving forces at 1250 and 1350 °C and the driving forces of the largest grains at the temperatures and duration times, Δg_{LG}^{T-t} , along with the grain growth rates with the driving forces.

3.2. Carbide Growth of VC-doped WC-Co

A slow heating rate of 10 °C/min was employed during heating for homogeneous distribution of V. FESEM micrographs of VC-doped WC-Co samples sintered at 1250, 1300 and 1350 °C for 1 h, respectively, are presented in Fig. 20a–c. Abnormal carbide was not observed in the samples sintered at 1250 and 1300 °C for 1h (see Fig. 20a and b), whereas some appeared in the samples sintered at 1350 °C for 1h, which are indicated by blue dashed polygons in Fig. 20c. Fig. 20d–f shows the variation in the carbide size distribution of the systems as a function of sintering temperature and time. Little change was noted at 1250 and 1300 °C with time and the carbide growth is minimal (see Fig. 20d and e). To my best knowledge so far, no such nanostructure with extremely small carbides has been reported. At 1350 °C, however, the carbide particles begin to grow abnormally from the early stage of sintering as shown in Fig. 20f. These imply that Δg_c of the system might be significantly large if the carbide growth occurs in the mixed-control mode. Interestingly, the growth kinetics of the abnormally-grown carbides as well as other nano-sized carbides in the system is considerably slow than that of pure WC-Co. The size of the abnormal carbides was in the range of several micrometers even though the number density of the abnormal carbides is very low compared with pure WC-Co (refer to Section 3.3.1). In addition, the surfaces of small WC carbides look relatively rough compared with that in pure WC-Co which is fully faceted (Fig. 18a and b vs. Fig. 20a and b), while the large particles have faceted surfaces as denoted by white arrows in Fig. 20a–c.

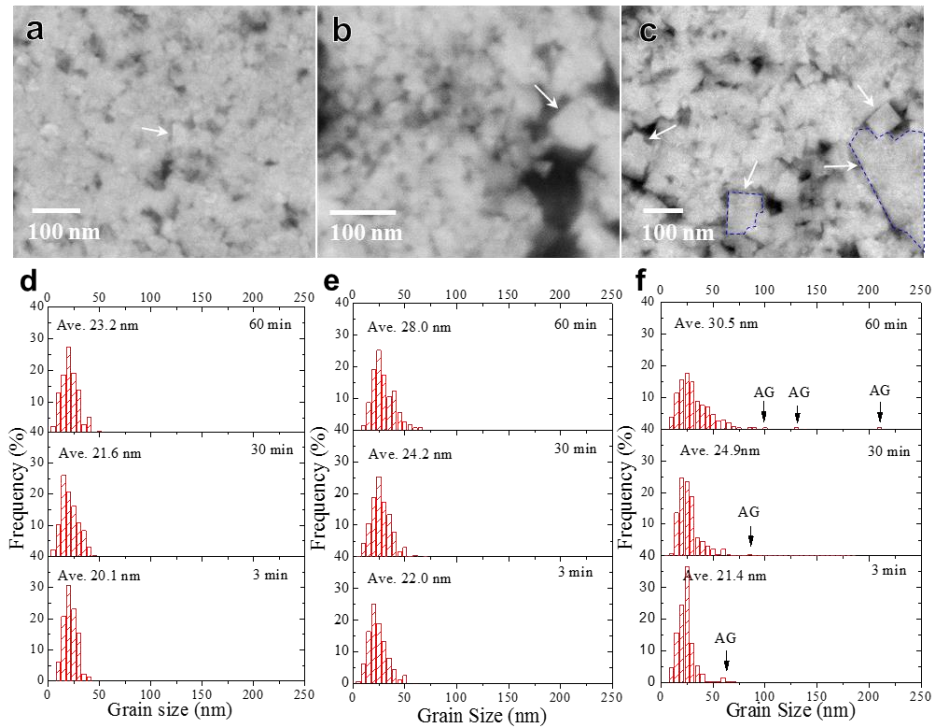


Figure 20. . FESEM images and grain size distribution for the VC-doped WC–Co samples sintered at various temperatures and times. Slow heating rate of 10 °C/min was employed in order to maximize the effect of grain growth inhibition: (a) 1250 °C for 1 h, (b) 1300 °C for 1 h, (c) 1350 °C for 1 h. (d), (e) and (f) show the variation of the particle size distribution at 1250, 1300 and 1350 °C, respectively, as a function of time. The grains with faceted interfaces are marked by white arrows.

Based on the results above, we can tentatively conclude that the carbide growth of the VC-doped WC–Co is delayed by the increase in Δg_c . But the slow growth kinetics of the abnormal carbides as well as small matrix carbides cannot be explained by the increase in Δg_c alone.

3.3. Interface Characterization: (V,W)C cubic layer formation

Cs-STEM studies were performed on the samples prepared by quenching to room temperature from 1200 °C after 1 h and representative results are summarized in Fig. 21. The shape of WC carbides is generally a triangular prism which consists of two $\{0001\}$ basal facets and three $\{10\bar{1}0\}$ prismatic facets [45, 53, 58]. Thus, we need to investigate the two habit planes regardless of the existence of steps since the steps also consist of the basal and prismatic facets [44, 53].

Fig. 21a shows a typical WC carbide in the sample, in which the center carbide is seen along $[0001]$ direction and the carbide denoted by white dashed square along the $[1\bar{2}10]$ direction. The carbide surfaces are very rough, which is well consisted with the FESEM images in section 3.3.2. This is closely related to the carbide growth behavior, which will be discussed later. Cs-HR STEM DF and BF images of the typical prismatic and basal interfaces are shown in Fig. 21b and c, respectively, which are from the region denoted by label A and B in Fig. 21a.

The dark, two atomic layers within white dashed square in Z-contrast image (Fig. 21b), correspond to a segregated (V,W)C on $(10\bar{1}0)$ facets. The elements in dark region of the DF image correspond to light element, while it is opposite in BF image. We found that most of the $\{10\bar{1}0\}$ facets of WC carbides, in this study, are uniformly covered by two atomic layers of (V,W)C, where the relationship of $(10\bar{1}0)_{WC} // (001)_{(V,W)C}$ exists at the interface as

illustrated in Fig. 21d. The interplanar distance of $(110)_{(V,W)C}$ is measured to be ~ 2.9167 Å, which is similar to that of VC, 2.9465 Å from JCPDs, while those of $(0001)_{WC}$ and $(1\bar{2}10)_{WC}$ near the interface are about 2.9234 and 3.0599 Å. Thus, the misfit at the interface can be estimated as 0.23 % along $[0001]$ direction and 5.71 % along $[0\bar{1}10]$ direction, respectively. In spite of the large misfit along $[0\bar{1}10]$ direction, they make a coherent interface in the long range as shown in Fig. 21b. Fig. 21c shows the (0001) basal facets, where the bright, three atomic layers are uniformly formed on it with $(0001)_{WC} // (111)_{(V,W)C}$ orientation relationship as shown in Fig. 21e. The interatomic distances on $(0001)_{WC}$ planes and $(111)_{(V,W)C}$ planes are measured to be 2.9714 Å and 2.9387 Å, respectively, with calculated lattice misfit of ~ 1.1 %. This low misfit might have induced three layers of atoms on the (0001) facets: i.e., low misfit at $(0001)_{WC} // (111)_{(V,W)C}$ interface compared with $(10\bar{1}0)_{WC} // (001)_{(V,W)C}$ interface.

The results are somewhat different from other reports, which show a thinner (two layers) (V,W)C layer on (0001) facets and a partial covering of $(10\bar{1}0)$ facets with the intermittent segregation of (V,W)C phase as an island type [51, 53, 56]. Sugiyama et al. [53] explained the morphology of the interface structures in terms of lattice misfits between WC and (V,W)C layer. This interpretation is in line with our results, but the different appearance of the morphologies in our results and their results cannot be explicitly understood.

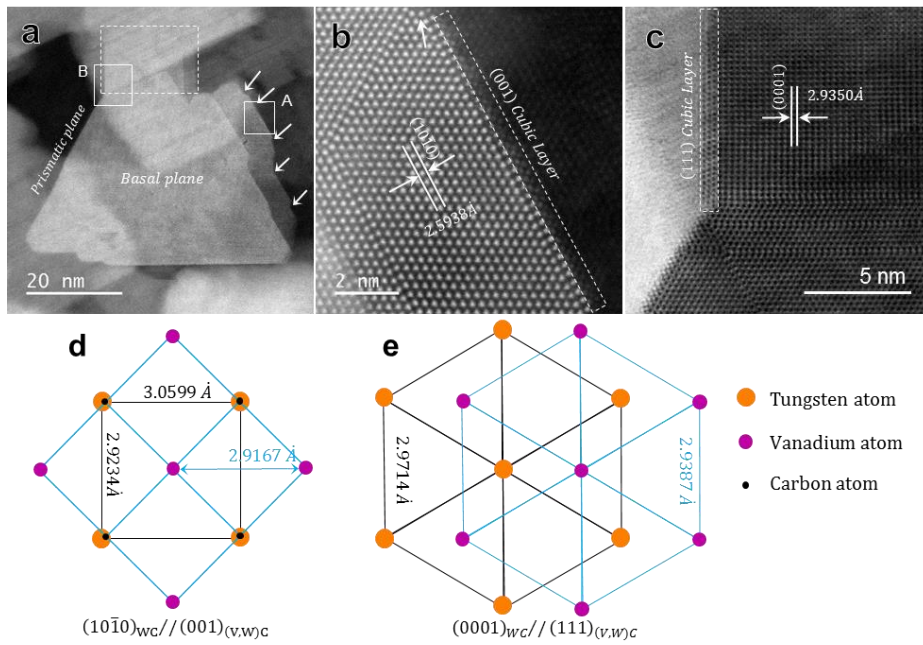


Figure 21. CS-STEM micrographs of VC-doped WC–Co sample prepared by quenching from 1200 °C after 1 h sintering: (a) STEM dark-field (DF) image showing WC grain analyzed, (b) high resolution (HR) STEM DF image illustrating the segregated (V,W)C atomic layers on (10 $\bar{1}$ 0) surface of WC in the region labeled A, (c) HR STEM bright-field (BF) image showing the the segregated (V,W)C atomic layers on (0001) surface of WC in the region labeled B. (d) and (e) illustrate the orientation relationship at the prismatic and basal interfaces, respectively.

In the growth of the cubic phase precipitating, the lattice misfit between a thin film cubic phase and WC substrate might induce a misfit dislocation and cracks in the thin film layer. Thus, there should be a critical number of atom layers which exist without a generation of misfit dislocation [85]. Similarly, there will be a critical atom layer of (V,W)C, which might be determined by the area of interface as well as the degrees of misfits. Once the lattice misfit accumulated at an interface approaches the critical value, the (V,W)C phase is likely to become a thinner layer or separate in an island form to reduce the strain developed at the interfaces.

The thick layers (three atomic layers) of (V,W)C were commonly observed only on (0001) facets of the small ledges less than about 10 nm, while the presence of thinner layers on large ledges [44, 45, 51, 55, 56] provides the evidence for the above supposition. In our system, it seems that many small steps at the surfaces of WC carbides (see the white arrows in Fig. 21a and b) make a possible to form the thicker and homogeneous layers. The existence of many steps in our system can prevent the system from the accumulation of misfit strain by introducing short range matches between WC and (V,W)C layers.

3.4. Formation of Twins and Ledges

While the unusual complete sealing of WC carbides by (V,W)C layers in the present study is elucidated by the existence of small steps at the surfaces of WC carbides, the knowledge of how the steps are formed and are distributed inside WC carbides is instructive in understanding the behavior of the constituent atoms and carbide growth during sintering. Interestingly, it is observed that there are many twins inside all WC carbides, which we have observed, as displayed in STEM DF image of Fig. 22a. Fig. 22b and c shows the enlarged STEM DF images illustrating the twins inside WC carbides (yellow arrows) and the steps at the surfaces of WC carbides (white dashed ellipses). The small steps are placed at the end of the twins, indicating that their origin is the twins inside WC carbides. The dark, defects inside WC carbides, which correspond to light elements in STEM DF images, are often observed, where the twins seem to initiate as denoted by yellow arrows in Fig. 22a and c. In order to identify the defects inside WC carbides, high resolution Cs STEM and STEM-EDS analysis were performed as presented in Fig. 22d–g. The $(10\bar{1}0)$ facets of WC carbides is covered with two atomic layers of (V,W)C layers and the dark atom, V, in the same Z-contrast for (V,W)C layers is trapped in the outmost layer of $(10\bar{1}0)$ facets as pointed by pink dashed ellipse in Fig. 22d. The twins are also observed at the vicinity of the dark atom (yellow arrows). Fig. 22e shows V composition mapping results corresponding to the region outlined by white square in Fig. 22d. V is mainly concentrated at the (V,W)C layers and interestingly, resided inside WC carbides rather than Co

phase. This result is absolutely unexpected when considered the fact that the solubility of V in WC is nearly zero [86] and V is mainly concentrated at the WC/Co interface and Co phase [53].

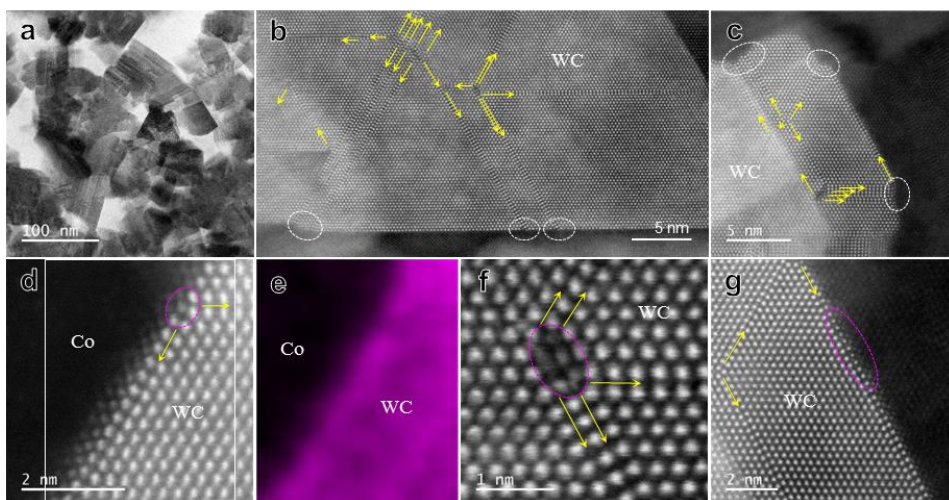


Figure 22. CS-STEM micrographs of VC-doped WC–Co sample prepared by quenching from 1200 °C after 1 h sintering; (a) STEM BF image showing WC grains with a high density of twins, (b) and (c) HR STEM DF image illustrating the array of twins inside WC grain and ledges on the surface of grain. (d) and (e) are HR STEM DF image and EDS result, respectively, showing the presence of V and the origin of twins. (f) demonstrates the trapped V cluster and (g) provides an evidence for the V or W diffusion through (V,W)C cubic layers. Yellow arrows indicate the twins and white dashed ellipses the ledges on the prismatic facets in (b) and (c). Pink ellipses in (d), (f) and (g) are for V atom and clusters trapped in WC grain.

Besides the dark atoms, dark clusters are often observed inside WC carbides as denoted by the pink dashed ellipse in Fig. 22f, which correspond to V atoms too. These results are in line with the STEM-EDS mapping results. Many twins are generated at the region of V cluster, which seems to come from the relaxation of V inside WC lattice. The V atom or cluster inside WC carbides is considered to be trapped during the carbide growth at the sintering stage because V is not included at the synthesis process of WC powder. The V trapping and twin generation are a rare event in the submicron-sized VC-doped WC-Co systems [44, 45, 51, 53, 55, 56], indicating that it is a unique feature of the nanostructured WC-Co with a small carbide size less than 100 nm.

The trapping of V and subsequent twin generation in the nano system can be explained by two possibilities. One is the trapping of V by a different growth rate of carbides with crystallographic directions. If the growth rate in a directions is dissimilar, the (V,W)C layers at the region growing slow can be partly trapped by the growth of the other region growing fast. The other possibility is that V atom or cluster is stabilized inside the WC lattice by generating twins. The twin generation in the system can be relatively easier than in submicron or micron-sized material system. Although twins have a low energy in the lattice, the formation of many twins through a long range will increase the energy of whole system, preventing the V trapping and the subsequent twin generation.

The trapping of V atoms during sintering provides not only the evidence for the existence of (V,W)C layers during sintering but also the clue for the carbide growth behavior when WC carbides are sealed with the (V,W)C

layers. It is observed that the outmost layer of WC carbide adjacent to the (V,W)C layers is partly occupied by some small and dark atoms as highlighted by pink dashed ellipse in Fig. 22g. These atoms by the Z-contrast image correspond to the V atoms that are trapped during growth when WC particles grow, whereas, these are the atoms occupied in the position of W atoms dissolved when WC particles shrink. It indicates that the growth of WC carbides is completed by the inward diffusion of W atoms via the (V,W)C layers after 2-DN.

3.5. Effect of Step Free Energy

Most interesting feature of the present system is that their nanostructure is highly stable to the carbide growth. Their carbide growth follows a discontinuous growth behavior by 2-DN and growth as presented in Section 3.2.2, which is attributed to the faceted character of WC carbide surfaces. In order to appreciate the origin of the high stability of the nanostructure, it is thus instructive to investigate the effects of the step free energy, the concentration of W atoms in Co phase, the diffusivity and the interfacial energy according to the Eqs. (29)–(31).

The critical driving force is mainly affected by the step free energy, σ , according to Eq. (31). It is reported that the σ can be changed by adding dopants[74, 78, 87, 88]. The dopant addition in these studies commonly induces the change of grain shape from rounded to faceted or vice versa, accompanied abnormal grain growth in faceted systems due to the increased 2-DN barrier. According to Wallace et al.[87], $\langle 111 \rangle$ twins exaggerate abnormal grain growth containing twins in lead magnesium niobate-lead titanate system because the twins decrease 2-DN barrier.

The present system showed a very high thermal stability even though they possess many twin-induced steps. This is thus distinctive from the variation in σ by the shape change as above mentioned reports because our system keeps still a faceted morphology and the reduction of σ is not perceived by the generation of steps. The deliberate observation for the steps in Fig. 22b–d provides the clue for the high stability. All the steps highlighted by

white or pink dashed ellipses are completely sealed with (V,W)C layers. The growth by 2-DN is recognized as a layer by layer growth. When W atoms precipitate on (V,W)C layer, newly formed layer of WC is likely to have (V,W)C form with a cubic structure. Thus, such a new layer formation induces an additional strain energy because the preformed two or three layers of (V,W)C will be in the equilibrium thickness as discussed in previous Section 3.2.4. In addition, the co-precipitation of W and V atoms is energetically favorable due to the large difference between W and V atomic radii. However, the lack of V in Co phase in Fig. 22e might make such a co-precipitation more difficult. Therefore, we can conclude that the existence of (V,W)C layers contributes to the rise of 2-DN barrier, i.e. the critical driving force, Δg_c , leading to the delay of the occurrence of abnormal carbide growth as presented in Section 3.2.2.

3.6. Effect of Solubility and Diffusivity of W

Although the delay of abnormal carbide growth is elucidated by the increase in Δg_c , the slow growth rate of the abnormal carbides (cf. Section 3.2.2) cannot be understood. According to Eq. (29), the growth rate of the growing carbides with a larger driving force than Δg_c is proportional to the concentration of W in the saturated Co solution, C_∞ , of which the original meaning is the equilibrium concentration for an infinite radius ($r = \infty$). STEM-EDS analysis was performed for the samples quenched at 1200 °C after 1 h. The equilibrium concentrations of the saturated Co-based solutions for the pure WC–Co and the VC-doped WC–Co specimens are listed in Table 1. According to the results, the concentration of W in the Co-based solution is not influenced by the addition of V, which is similar to the results reported by Lavergne et al.[89] as listed in Table 1. They also reported that the diffusivity of W in Co-based solution, D_W^{Co} , is not affected by V addition at 1200 °C. These results indicate that the slow carbide growth of the present system is not a matter of the solubility and diffusivity of W in Co phase at the concerned temperature range.

3.7. Effect of Interfacial Energy

According to Eq. (29), the change of the interfacial energy can also influence the growth rate of the growing carbides. Johansson et al., performed the theoretical work for the interfacial energetics of the VC-doped WC–Co system. Their work showed that the V segregation as a thin film is stable for a wide range of temperatures and the interfacial energy can be decreased by minimally 0.05J/m^2 and maximally 1.1J/m^2 by (V,W)C thin film at WC/Co interface. However, this amount of the interfacial energy decrease is negligible compared with the decrease in the growth rate less than one hundredth of the present system (cf. Section 3.2.2). The another reason related to the (V,W)C layers will thus be in control for the carbide growth inhibition.

3.8. Modeling of Carbide Growth of VC-doped WC–Co system

We suggest the carbide growth mechanism of the present system by the interference of the (V,W)C layers based on the above results. The growth of WC carbides in the system is eventually completed by the infiltration of W atoms through (V,W)C layers after 2-DN on the layer. This means that 2-DN of W atoms on (V,W)C layers is not the completion of growth. The evidence for the diffusion of W atoms through (V,W)C layers is found in Fig. 22g as presented in Section 3.2.4. Hence, the carbide growth of the system is considered as the mixed control of 2-DN on (V,W)C layer and the diffusion through the layers.

In order for this supposition to be valid, it should be first verified that all of the WC grains in this system can be fully covered with the (V,W)C cubic layers by the addition of 1.5 wt % VC. Based on the experimental observation as presented in Section 3.2.2 and 3.2.3, the shape of WC grains was assumed to be triangular prism with an aspect ratio of $h/t = 1$ as shown in Figure 23a. It is also considered that three atomic layers and two atomic layers of (V,W)C cubic phase are precipitated on $\{0001\}$ basal facets and $\{10\bar{1}0\}$ prismatic facets, respectively. Figure 23b shows the estimated numbers of WC grains and the WC grains to be covered with the (V,W)C cubic layers.

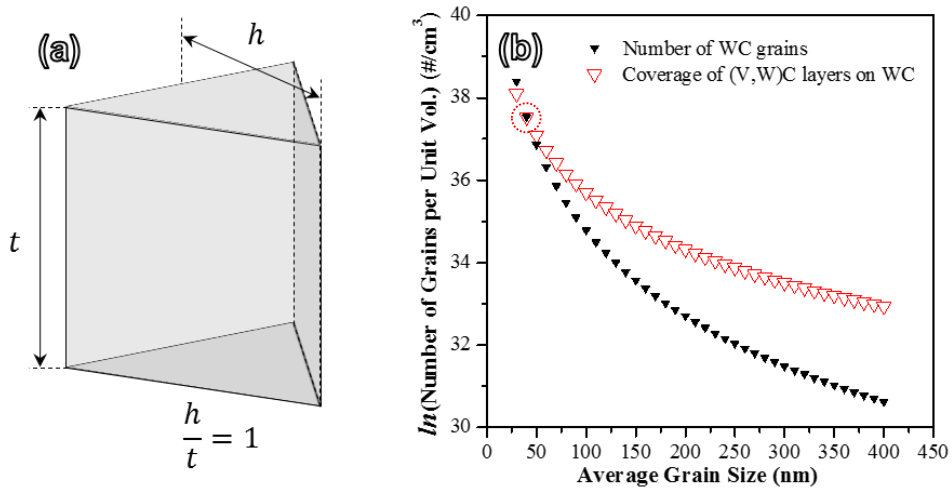


Figure 23. The estimated numbers of WC grains per unit volume and the numbers of WC grains per unit volume, which can be covered by (V,W)C cubic layers, with grain size. (a) schematic diagram of WC grain, (b) The calculated results.

The Numbers of both WC grains (black triangles) and WC grains to be covered with (V,W)C cubic layers (red open triangles) were exponentially decreased with increase in grain size. The numbers of WC grains per unit volume were larger than that of WC grains to be covered with (V,W)C cubic layers below 30 nm of average grain size, which is a critical size that the numbers of WC grains are equal to the numbers of WC grains to be covered with (V,W)C cubic layers (red dotted circle in Figure 23b), while become smaller above 30 nm. These results reveals that WC grains in our system can be fully covered with (V,W)C cubic layers and the amounts of VC dopants should be determined by WC grain size used. Thus, it can be said that the supposition above is valid.

Figure 24 illustrates the concentration profile of W through the phases and the 2-DN and the diffusion of W atoms through the (V,W)C layers.

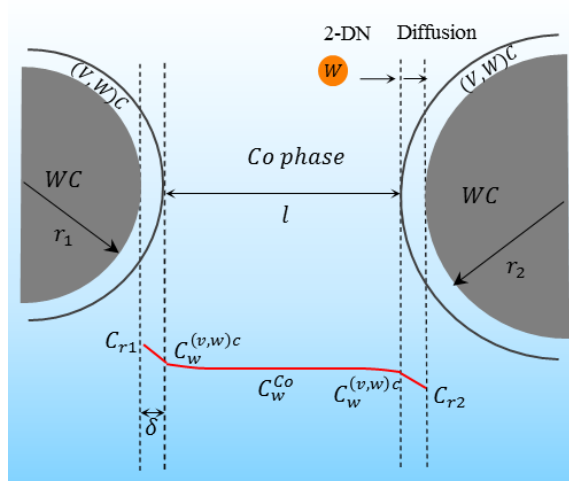


Figure 24. Schematic illustration of the concentration profile of W through the phases and 2-DN on (V,W)C layer, through which W diffusion occurs.

To consider the diffusion through (V,W)C layers, we assume the steady-state diffusion through concentric spheres of radii r and $r + \delta$, which is the same as that proposed for the diffusion of carbon in tungsten ball by Pirani and Sandor[37]. The mathematical expression of the model is described as

$$\frac{d}{dR} \left(R^2 \frac{dC}{dR} \right) = 0 \quad (33)$$

where C is the concentration at radius R . If we apply the boundary condition for the above Eq. (6), the flux is expressed as

$$J(r) = -D \frac{dC}{dr} = \frac{D_W^{(V,W)C}}{r^2} \frac{(C_w^{(v,w)c} - C_r)}{\left(\frac{1}{r + \delta} - \frac{1}{r} \right)} \quad (34)$$

where $D_W^{(V,W)C}$ is the diffusivity of W in (V,W)C layers, C_r the concentration of W at the WC/(V,W)C interface of WC with a radius r , $C_w^{(v,w)c}$ the concentration of W at the (V,W)C/Co interface, δ the thickness of (V,W)C

layers. The growth rate is expressed as

$$\frac{dr}{dt} = \frac{D_W^{(V,W)C}}{r^2} \frac{(C_W^{(v,w)C} - C_r)}{\left(\frac{1}{r+\delta} - \frac{1}{r}\right)} \quad (35)$$

where $C_W^{(v,w)C}$ is similar to the concentration of W at very large distances from WC carbide, C_W^{Co} , according to STEM-EDS analysis. If The term $C_W^{(v,w)C} - C_r \approx C_W^{Co} - C_r$ is written as $(C_W^{Co} - C_\infty) - (C_r - C_\infty)$ and the Gibbs-Thomson relation is applied,

$$C_r - C_\infty = \frac{2\gamma V_m C_\infty}{RT r} \quad (36)$$

$$C_W^{Co} - C_\infty = \frac{2\gamma V_m C_\infty}{RT r^*} \quad (37)$$

where C_∞ and r^* have a same meaning in Eqs. (39) and (30). Eq. (35) can then be expressed as

$$v'_D = \frac{dr}{dt} = \frac{2\gamma V_m C_\infty D_W^{(V,W)C}}{RT r^2 \left(\frac{1}{r+\delta} - \frac{1}{r}\right)} \left(\frac{1}{r^*} - \frac{1}{r}\right) \quad (38)$$

This equation is similar to Eq. (29) derived by Ardell for form's sake. Comparing Eq. (38) with Eq. (29), it can be noticed that the growth rate is limited by a low diffusivity of W in (V,W)C layer, $D_W^{(V,W)C}$, which might be several orders lower than that in Co phase, and the thicker the thickness of (V,W)C layer is, the slower the growth rate is.

Thus, the carbide growth rate of the present system is controlled by a mixed manner of 2-DN on (V,W)C layer and the diffusion through the layers and expressed as similar to Eq. (28).

$$v_M \equiv \frac{dr}{dt} = \left(\frac{1}{v'_R} + \frac{1}{v'_D} \right)^{-1} \quad (39)$$

where v'_R has a same formula with Eq. (30), but a different step free energy value, σ' .

In conclusion, the most interesting feature of the present system is the high stability of extremely fine nanostructure for a long time-at-temperature up to high temperature, providing possibly scalable pathway, which may be understood as follows.

The finer the size of WC carbides is, the faster the carbide growth is, which is governed by accelerated abnormal carbide growth. However, the WC carbides of the present system is completely sealed with (V,W)C layers, which is enabled by the many twin-induced steps. The abnormal growth of nano WC carbides is prevented due to the increased strain energy by an additional layer formation through 2-DN on (V,W)C, and the growth rate of growing carbides is also limited by the diffusion of W atoms through (V,W)C layers.

3.9. Synthesis of nano WC-Co via liquid phase sintering

In order to demonstrate the realizable possibility for the mass production of nanostructured WC-Co composites, the variation of the relative densities and WC particle size of VC-doped WC-Co composites with temperature and time during liquid phase sintering were examined. The resulting density variations and particle sizes are presented in Figure 25. Here, the theoretical density is roughly estimated by the mixture rule and the estimated value is 14.55 g cm^{-3} . At 1250°C , the relative density and WC particle size were initially 76.4 % and 20.1 nm, respectively, and rarely changed with time. On the other hand, the relative densities at 1300 and 1350°C were initially 79.0 and 83.2 %, respectively, and dramatically increased to 94.4 and 97.0 %, respectively, while the WC particles were merely grown up to 2 h holding. These results reveal that the nanostructured WC-Co composites with a size of $\sim 30 \text{ nm}$ can be achievable if pressure-assisted sintering such as gas pressure sintering (GPS), which is widely used in cutting tool manufacturers, is adopted.

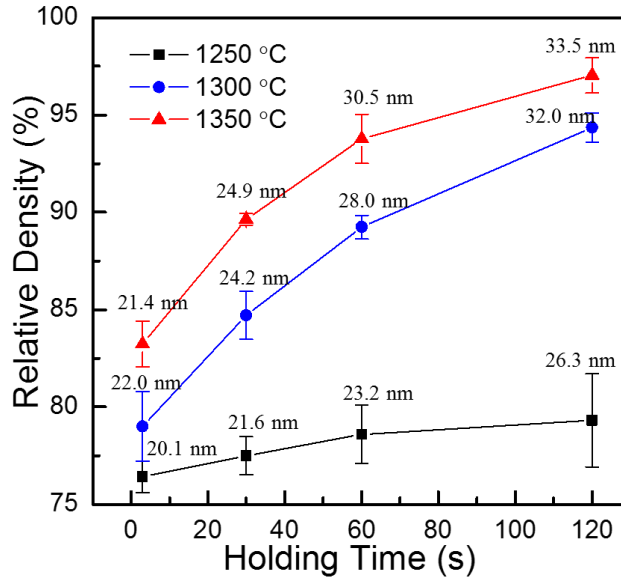


Figure 25. The variation of the relative densities and WC particle sizes with temperature and time during liquid phase sintering.

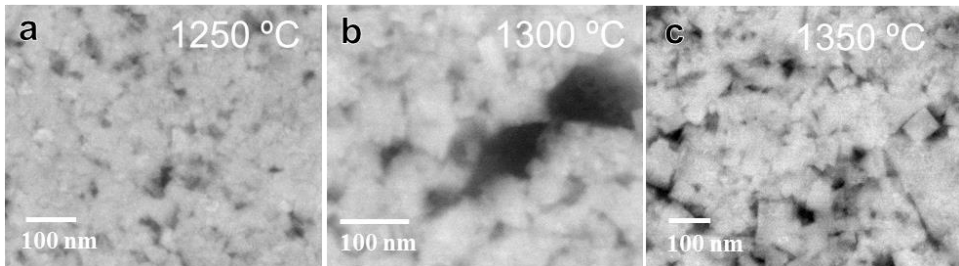


Figure 26. FESEM micrographs for the samples sintered at 1250 (a), 1300 (b) and 1350 °C (c) for 1h, respectively.

Figure 26a, b and c show FESEM micrographs for the samples sintered at 1250, 1300 and 1350 °C for 1h, respectively. The samples sintered at 1250 and 1300 °C for 1h have small particle sizes and homogeneous size distributions (Figure 26a and b). At 1350 °C, abnormal WC particles begin to appear as shown in Figure 26c, which might be related to the decrease in thermodynamic stability of (V,W)C cubic layers. According to the theoretical study of Johansson and Wahnstrom[52], the thermodynamic stability of (V,W)C cubic decreases with temperature.

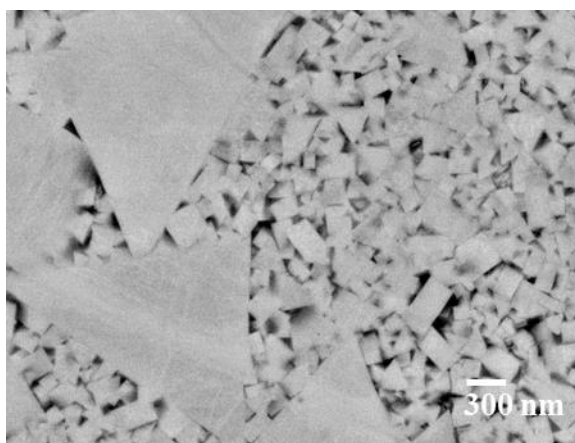


Figure 27. FESEM micrograph of the sample heated to 1300 °C at a heating rate of 100 °C/min and held at the temperature for 1 min.

It was found that the growth behavior of WC particles is changed with a heating rate during heating stage of sintering. Figure 27 shows FESEM micrograph of the sample heated to 1300 °C at a heating rate of 100 °C/min and held at the temperature for 1 min. WC particle size was very large compared with the samples heated at a heating rate of 10 °C/min. Moreover, very large abnormal particles were frequently observed. This somewhat unexpected result could be attributed to the lack of time for the homogeneous distribution of VC through the specimen during heating, which additionally supports our supposition for the mechanism of grain growth inhibition. From the result, the techniques with a fast heating rate is not suitable for the sintering of VC-doped WC–Co composites because WC particles can grow fast before the complete sealing of (V,W)C layers.

IV. Conclusion

A systematic analysis of the carbide growth behavior during sintering was performed with nanostructured VC-doped WC–Co system. Following are the summary and conclusions of this study:

1. The carbide growth of pure WC–Co system with a small carbide size is highly accelerated due to the large driving force for growing carbides by AGG.
2. VC-doped WC-Co system exhibited very high thermal stability of nanostructures for a long time-at-temperature up to high temperatures.
3. Three and two atomic layers of (V,W)C phase were found to be uniformly segregated on (0001) and (10 $\bar{1}$ 0) facets of WC, respectively. V atoms mainly resided at the WC/Co interface and inside WC carbides, but are not in the Co phase, which is attributed to the segregation and trapping of V atoms during carbide growth.
4. Trapped V atoms generated many twins in order to relax itself inside WC carbides, accompanying the subsequent generation of many steps. The steps assist the complete sealing of nano WC carbides by (V,W)C layers, leading to the effective inhibition of carbide growth.

Overall Conclusion

The formation of WC nanopowder during carbothermal reduction and the grain growth inhibition of WC particles during liquid phase sintering were systematically explored both experimentally and theoretically. New methodology for the fabrication of various nanopowders was developed and the scalable possibility of nanostructured WC–Co composites with an extremely fine particle size of 30 nm was suggested. The main results can be summarized as follows:

First, extremely fine WC nanopowder with an average grain size of 10.54 nm was successively synthesized by newly developed production method, grain growth controlled method. The carbothermal reduction of $\text{WO}_3\text{-C}$ mixture is controlled by the outward diffusion reaction of oxygen and the inward diffusion reaction of carbon in reactant grains. A theoretical estimation for the reactions during carbothermal reduction reveals that the smaller the grain size is, the faster the reactions are. The experimental results for the growth of WC grains is fitted by linear regression between the cube of average grain size (\bar{a}^3) and time (t). A theoretical approach for the grain growth represents that the growth of WC grains is mainly controlled by the surface diffusion, and the average grain size is proportional to $\sim t^{0.32}$. The grain growth rate increases with the coordination number, revealing that the loose packing of raw powder mixture during carbothermal reduction is beneficial for the fabrication of nanopowders.

Second, a systematic analysis of the carbide growth behavior during sintering was performed with nanostructured VC-doped WC–Co system. Three and two atomic layers of (V,W)C phase were found to be homogeneously segregated on (0001) and (10 $\bar{1}$ 0) facets of WC, respectively. V atoms mainly resided at the WC/Co interface and inside WC carbides, but are not in the Co phase, which is attributed to the segregation and trapping of V atoms during carbide growth. Trapped V atoms generated many twins in order to relax itself inside WC carbides, accompanying the subsequent generation of many steps. The steps assist the complete sealing of nano WC carbides by (V,W)C layers, leading to the effective inhibition of carbide growth. VC-doped WC–Co system exhibited very high thermal stability of nanostructures for a long time-at-temperature up to high temperatures (1300 °C for 1 h), which guarantees the possibilities of the mass production of the genuine nanostructured WC–Co composites (30 nm in an average particles size).

Reference

- [1] Z.Z. Fang, X. Wang, T. Ryu, K.S. Hwang, H. Sohn. Synthesis, sintering, and mechanical properties of nanocrystalline cemented tungsten carbide—a review, *International Journal of Refractory Metals and Hard Materials* 27 (2009) 288–299.
- [2] F. Medeiros, S. De Oliveira, C. De Souza, A. Da Silva, U. Gomes, J. De Souza. Synthesis of tungsten carbide through gas–solid reaction at low temperatures, *Materials Science and Engineering: A* 315 (2001) 58–62.
- [3] H. Fecht. Synthesis and properties of nanocrystalline metals and alloys prepared by mechanical attrition, *Nanostructured Materials* 1 (1992) 125–130.
- [4] M. Xueming, Z. Ling, J. Gang, D. Yuanda. Preparation and structure of bulk nanostructured WC–Co alloy by high energy ball-milling, *Journal of materials science letters* 16 (1997) 968–970.
- [5] R. Uribe, C. Baudin, L. Mazerolles, D. Michel. Sub-micron sized Al_2TiO_5 powders prepared by high-energy ball milling, *Journal of materials science* 36 (2001) 5105–5113.
- [6] F. Zhang, C. Wang, M. Zhu. Nanostructured WC/Co composite powder prepared by high energy ball milling, *Scripta materialia* 49 (2003) 1123–1128.
- [7] R. Porat, S. Berger, A. Rosen. Sintering behavior and mechanical properties of nanocrystalline WC/Co. *Materials Science Forum*, vol. 225: Trans Tech Publ, 1996. p.629–648.
- [8] H. Fecht, E. Hellstern, Z. Fu, W. Johnson. Nanocrystalline metals prepared by high-energy ball milling, *Metallurgical Transactions A* 21 (1990) 2333.
- [9] Z. Ban, L. Shaw. On the reaction sequence of WC–Co formation using an integrated mechanical and thermal activation process, *Acta materialia* 49 (2001) 2933–2939.
- [10] Z.-G. Ban, L. Shaw. Synthesis and processing of nanostructured WC–Co materials, *Journal of Materials Science* 37 (2002) 3397–3403.
- [11] W. Liu, X. Song, J. Zhang, G. Zhang, X. Liu. Preparation of ultrafine WC–Co composite powder by in situ reduction and

carbonization reactions, *International Journal of Refractory Metals and Hard Materials* 27 (2009) 115–120.

[12] L. McCandlish, B. Kear, B. Kim. Processing and properties of nanostructured WC-Co, *Nanostructured Materials* 1 (1992) 119–124.

[13] L.E. McCandlish, B.H. Kear, S.J. Bhatia. Spray conversion process for the production of nanophase composite powders. Google Patents, 1994.

[14] G.E. Spriggs. A history of fine grained hardmetal, *International Journal of Refractory Metals and Hard Materials* 13 (1995) 241–255.

[15] L. Gao, B. Kear, P. Seegopaul. Method of forming tungsten carbide particles. Google Patents, 1999.

[16] P. Seegopaul, L. Gao. Method of forming nanograin tungsten carbide and recycling tungsten carbide. Google Patents, 2003.

[17] B.-K. Kim, G.-H. Ha, Y.-W. Woo. Method of production WC/Co cemented carbide using grain growth inhibitor. Google Patents, 2003.

[18] G.-G. Lee, G.-H. Ha, B.-K. Kim. Synthesis of nanostructure W base composite powders by chemical processes, *Journal of the Korean Institute of Metals and Materials*(South Korea) 37 (1999) 1233–1237.

[19] Z. Zhang, S. Wahlberg, M. Wang, M. Muhammed. Processing of nanostructured WC-Co powder from precursor obtained by co-precipitation, *Nanostructured Materials* 12 (1999) 163–166.

[20] M.T. Swihart. Vapor-phase synthesis of nanoparticles, *Current Opinion in Colloid & Interface Science* 8 (2003) 127–133.

[21] J. Hojo, T. Oku, A. Kato. Tungsten carbide powders produced by the vapor phase reaction of the WCl_6 - CH_4 - H_2 system, *Journal of the Less Common Metals* 59 (1978) 85–95.

[22] M. Fitzsimmons, V.K. Sarin. Comparison of WCl_6 - CH_4 - H_2 and WF_6 - CH_4 - H_2 systems for growth of WC coatings, *Surface and Coatings Technology* 76 (1995) 250–255.

[23] J. Kim, B. Kim. Synthesis of nanosized tungsten carbide powder by the chemical vapor condensation process, *Scripta materialia* 50 (2004) 969–972.

[24] X. Tang, R. Haubner, B. Lux, B. Kieffer. Preparation of ultrafine CVD WC powders deposited from WCl_6 gas mixtures, *Le Journal de Physique IV* 5 (1995) C5-1013–C1015–1020.

[25] C.-W. Won, B.-S. Chun, H. Sohn. Preparation of ultrafine

tungsten carbide powder by CVD method from $\text{WCl}_6\text{-C}_2\text{H}_2\text{-H}_2$ mixtures, *Journal of materials research* 8 (1993) 2702–2708.

[26] G. Leclercq, M. Kamal, J.M. Giraudon, P. Devassine, L. Feigenbaum, L. Leclercq, A. Frennet, J.M. Bastin, A. Löfberg, S. Decker. Study of the preparation of bulk powder tungsten carbides by temperature programmed reaction with $\text{CH}_4\text{-H}_2$ mixtures, *Journal of catalysis* 158 (1996) 142–169.

[27] L. Gao, B. Kear. Low temperature carburization of high surface area tungsten powders, *Nanostructured materials* 5 (1995) 555–569.

[28] H.Y. Sohn, T. Ryu, J.W. Choi, K.S. Hwang, G. Han, Y.J. Choi, Z.Z. Fang. The chemical vapor synthesis of inorganic nanopowders, *JOM* 59 (2007) 44–49.

[29] S.R. Vallance, S. Kingman, D.H. Gregory. Ultrarapid materials processing: Synthesis of tungsten carbide on subminute timescales, *Advanced Materials* 19 (2007) 138–142.

[30] G.-L. Tan, X.-J. Wu. Mechanochemical synthesis of nanocrystalline tungsten carbide powders, *Powder metallurgy* 41 (1998) 300–302.

[31] M.S. El-Eskandarany, A.A. Mahday, H. Ahmed, A. Amer. Synthesis and characterizations of ball-milled nanocrystalline WC and nanocomposite WC-Co powders and subsequent consolidations, *Journal of Alloys and Compounds* 312 (2000) 315–325.

[32] J. Kim, S. Kang. WC platelet formation via high-energy ball mill, *International Journal of Refractory Metals and Hard Materials* 47 (2014) 108–112.

[33] M.R. Andrews. Production and characteristics of the carbides of tungsten, *The Journal of Physical Chemistry* 27 (1923) 270–283.

[34] M.R. Andrews. Diffusion of carbon through tungsten and tungsten carbide, *The Journal of Physical Chemistry* 29 (1925) 462–472.

[35] L.V. McCarty, R. Donelson. A diffusion model for tungsten powder carburization, *Metallurgical Transactions A* 18 (1987) 969–974.

[36] S. Kharatyan, H. Chatilyan, L. Arakelyan. Kinetics of tungsten carbidization under non-isothermal conditions, *Materials Research Bulletin* 43 (2008) 897–906.

[37] M. Pirani, J. Sandor. Diffusion of carbon into tungsten, *JOURNAL OF THE INSTITUTE OF METALS* 73 (1947) 385–&.

[38] W. Coblenz, J. Dynys, R. Cannon, R. Coble. Initial stage

solid state sintering models. A critical analysis and assessment, *Sintering Processes. Materials Science Research* 13 (1980) 141–157.

[39] S.-J.L. Kang. *Sintering: densification, grain growth and microstructure*, Butterworth-Heinemann, 2004.

[40] M. Ashby. A first report on sintering diagrams, *Acta Metallurgica* 22 (1974) 275–289.

[41] G.C. Kuczynski. Self-diffusion in sintering of metallic particles, *AIME TRANS* 185 (1949) 169–178.

[42] X. Wang, Z.Z. Fang, H.Y. Sohn. Grain growth during the early stage of sintering of nanosized WC-Co powder, *International Journal of Refractory Metals and Hard Materials* 26 (2008) 232–241.

[43] A. Jaroenworarluck, T. Yamamoto, Y. Ikuhara, T. Sakuma, T. Taniuchi, K. Okada, T. Tanase. Segregation of vanadium at the WC/Co interface in VC-doped WC-Co, *Journal of materials research* 13 (1998) 2450–2452.

[44] S. Lay, S. Hamar-Thibault, A. Lackner. Location of VC in VC, Cr₃C₂ codoped WC-Co cermets by HREM and EELS, *International Journal of Refractory Metals and Hard Materials* 20 (2002) 61–69.

[45] S. Lay, J. Thibault, S. Hamar-Thibault. Structure and role of the interfacial layers in VC-rich WC-Co cermets, *Philosophical Magazine* 83 (2003) 1175–1190.

[46] M. Kawakami, O. Terada, K. Hayashi. Effect of sintering cooling rate on V segregation amount at WC/Co interface in VC-doped WC-Co fine-grained hardmetal, *粉体および粉末冶金* 51 (2004) 576–585.

[47] M. Kawakami. Segregation Amount of Dopants at WC/Co Interface in Cr₃C₂-and VC+ Cr₃C₂-doped WC-Co Submicro-grained Hardmetals. *Proc. 16th Int. Plansee Seminar*, 2005, vol. 2: Plansee AG, 2005. p.653–667.

[48] M. Kawakami, O. Terada, K. Hayashi. A consideration on segregation process of dopant at WC/Co and WC/WC interfaces in VC doped WC-Co submicro-grained hardmetal. *The 2006 Powder Metallurgy World Congress & Exhibition*, 2006. p.334–335.

[49] J. Weidow, H.-O. Andrén. Grain and phase boundary segregation in WC-Co with small V, Cr or Mn additions, *Acta Materialia* 58 (2010) 3888–3894.

[50] S. Johansson, G. Wahnström. A computational study of thin cubic carbide films in WC/Co interfaces, *Acta Materialia* 59 (2011) 171–181.

-
- [51] I. Sugiyama, Y. Mizumukai, T. Taniuchi, K. Okada, F. Shirase, T. Tanase, Y. Ikuhara, T. Yamamoto. Formation of (W, V) C x layers at the WC/Co interfaces in the VC-doped WC-Co cemented carbide, *International Journal of Refractory Metals and Hard Materials* 30 (2012) 185–187.
- [52] S. Johansson, G. Wahnström. First-principles study of an interfacial phase diagram in the V-doped WC-Co system, *Physical Review B* 86 (2012) 035403.
- [53] I. Sugiyama, Y. Mizumukai, T. Taniuchi, K. Okada, F. Shirase, T. Tanase, Y. Ikuhara, T. Yamamoto. Three-dimensional morphology of (W, V) Cx in VC-doped WC-Co hard metals, *Scripta Materialia* 69 (2013) 473–476.
- [54] M. Kawakami, K. Kitamura. Segregation layers of grain growth inhibitors at WC/WC interfaces in VC-doped submicron-grained WC-Co cemented carbides, *International Journal of Refractory Metals and Hard Materials* 52 (2015) 229–234.
- [55] I. Sugiyama, Y. Mizumukai, T. Taniuchi, K. Okada, F. Shirase, T. Tanase, Y. Ikuhara, T. Yamamoto. Carbon content dependence of grain growth mode in VC-doped WC-Co hardmetals, *International Journal of Refractory Metals and Hard Materials* 52 (2015) 245–251.
- [56] K. Okada, A. Osada. Microstructural study on the grain growth inhibition of VC-doped WC-Co cemented carbides, *International Journal of Refractory Metals and Hard Materials* (2016).
- [57] W. Guo, K. Li, Y. Du, Z. Zhang, T. Xu, C. Yin, Z. Zhang, P. Zhou, X. Liu, B. Huang. Microstructure and composition of segregation layers at WC/Co interfaces in ultrafine-grained cemented carbides co-doped with Cr and V, *International Journal of Refractory Metals and Hard Materials* 58 (2016) 68–73.
- [58] H.R. Lee, D.J. Kim, N.M. Hwang, D.Y. Kim. Role of vanadium carbide additive during sintering of WC-Co: mechanism of grain growth inhibition, *Journal of the American ceramic society* 86 (2003) 152–154.
- [59] M. Elfving, S. Norgren. Study of solid-state sintered fine-grained cemented carbides, *International Journal of Refractory Metals and Hard Materials* 23 (2005) 242–248.
- [60] X. Song, Y. Gao, X. Liu, C. Wei, H. Wang, W. Xu. Effect of interfacial characteristics on toughness of nanocrystalline cemented carbides, *Acta Materialia* 61 (2013) 2154–2162.
- [61] C. Lin, E. Kny, G. Yuan, B. Djuricic. Microstructure and properties of ultrafine WC-0.6 VC-10Co hardmetals densified by

pressure-assisted critical liquid phase sintering, *Journal of alloys and compounds* 383 (2004) 98–102.

[62] L. Sun, C.-C. Jia, M. Xian. A research on the grain growth of WC-Co cemented carbide, *International Journal of Refractory Metals and Hard Materials* 25 (2007) 121–124.

[63] I. Azcona, A. Ordonez, J. Sanchez, F. Castro. Hot isostatic pressing of ultrafine tungsten carbide-cobalt hardmetals, *Journal of materials science* 37 (2002) 4189–4195.

[64] S. Zhao, X. Song, J. Zhang, X. Liu. Effects of scale combination and contact condition of raw powders on SPS sintered near-nanocrystalline WC-Co alloy, *Materials Science and Engineering: A* 473 (2008) 323–329.

[65] D. Sivaprahasam, S. Chandrasekar, R. Sundaresan. Microstructure and mechanical properties of nanocrystalline WC-12Co consolidated by spark plasma sintering, *International Journal of Refractory Metals and Hard Materials* 25 (2007) 144–152.

[66] S. Huang, L. Li, K. Vanmeensel, O. Van der Biest, J. Vleugels. VC, Cr₃C₂ and NbC doped WC-Co cemented carbides prepared by pulsed electric current sintering, *International Journal of Refractory Metals and Hard Materials* 25 (2007) 417–422.

[67] X. Yingfang, W. Xingqing, C. Lidong, L. Xiaodong, G. Hailiang. Preparation of superfine-cemented carbide by spark plasma sintering, *Journal of Wuhan University of Technology-Mater. Sci. Ed.* 21 (2006) 42.

[68] L. Zhu, Q. Huang, H. Zhao. Preparation of nanocrystalline WC-10Co-0.8 VC by spark plasma sintering, *Journal of materials science letters* 22 (2003) 1631–1633.

[69] S.I. Cha, S.H. Hong, B.K. Kim. Spark plasma sintering behavior of nanocrystalline WC-10Co cemented carbide powders, *Materials Science and Engineering: A* 351 (2003) 31–38.

[70] H.-C. Kim, I.-J. Shon, I.-K. Jeong, I.-Y. Ko, J.-K. Yoon, J.-M. Doh. Rapid sintering of ultra fine WC and WC-Co hard materials by high-frequency induction heated sintering and their mechanical properties, *Metals and Materials International* 13 (2007) 39–45.

[71] A. Michalski, D. Siemiaszko. Nanocrystalline cemented carbides sintered by the pulse plasma method, *International Journal of Refractory Metals and Hard Materials* 25 (2007) 153–158.

[72] E.M. Dubensky, R.T. Nilsson. Dense fine grained monotungsten carbide-transition metal cemented carbide body and preparation thereof. Google Patents, 1998.

[73] X. Wang, Z. Fang, H. Sohn. Nanocrystalline cemented

tungsten carbide sintered by an ultra-high-pressure rapid hot consolidation process, *Advances in Powder Metallurgy and Particulate Materials* 2 (2007) 08.

[74] H. Moon, B.-K. Kim, S.-J.L. Kang. Growth mechanism of round-edged NbC grains in Co liquid, *Acta materialia* 49 (2001) 1293-1299.

[75] B.-K. Yoon, B.-A. Lee, S.-J.L. Kang. Growth behavior of rounded (Ti, W) C and faceted WC grains in a Co matrix during liquid phase sintering, *Acta materialia* 53 (2005) 4677-4685.

[76] Y.-I. Jung, S.-Y. Choi, S.-J.L. Kang. Effect of oxygen partial pressure on grain boundary structure and grain growth behavior in BaTiO₃, *Acta materialia* 54 (2006) 2849-2855.

[77] K.S. Moon, S.J.L. Kang. Coarsening Behavior of Round-Edged Cubic Grains in the Na_{1/2}Bi_{1/2}TiO₃-BaTiO₃ System, *Journal of the American Ceramic Society* 91 (2008) 3191-3196.

[78] Y.-I. Jung, S.-J.L. Kang, D.Y. Yoon. Coarsening of polyhedral grains in a liquid matrix, *Journal of Materials Research* 24 (2009) 2949-2959.

[79] S.J.L. Kang, M.G. Lee, S.M. An. Microstructural evolution during sintering with control of the interface structure, *Journal of the American Ceramic Society* 92 (2009) 1464-1471.

[80] D.Y. Yang, D.Y. Yoon, S.J.L. Kang. Suppression of Abnormal Grain Growth in WC-Co via Two-Step Liquid Phase Sintering, *Journal of the American Ceramic Society* 94 (2011) 1019-1024.

[81] S.-M. An, S.-J.L. Kang. Boundary structural transition and grain growth behavior in BaTiO₃ with Nd₂O₃ doping and oxygen partial pressure change, *Acta Materialia* 59 (2011) 1964-1973.

[82] S.-H. Jung, S.-J.L. Kang. Repetitive grain growth behavior with increasing temperature and grain boundary roughening in a model nickel system, *Acta Materialia* 69 (2014) 283-291.

[83] A. Ardell. The effect of volume fraction on particle coarsening: theoretical considerations, *Acta metallurgica* 20 (1972) 61-71.

[84] J.M. Howe. *Interfaces in materials*, (1997).

[85] J. Matthews, A. Blakeslee. Defects in epitaxial multilayers: I. Misfit dislocations, *Journal of Crystal Growth* 27 (1974) 118-125.

[86] J. Weidow, S. Johansson, H.O. Andrén, G. Wahnström. Transition metal solubilities in WC in cemented carbide materials, *Journal of the American Ceramic Society* 94 (2011) 605-610.

[87] J.S. Wallace, J.M. Huh, J.E. Blendell, C.A. Handwerker.

Grain growth and twin formation in 0.74 PMN· 0.26 PT, Journal of the American Ceramic Society 85 (2002) 1581–1584.

[88] K. Choi, N.M. Hwang, D.Y. Kim. Effect of Grain Shape on Abnormal Grain Growth in Liquid-Phase-Sintered Nb_{1-x}Ti_xC–Co Alloys, Journal of the American Ceramic Society 85 (2002) 2313–2318.

[89] O. Lavergne, F. Robaut, F. Hodaj, C. Allibert. Mechanism of solid-state dissolution of WC in Co-based solutions, Acta materialia 50 (2002) 1683–1692.

국문초록

WC-Co 복합소재는 뛰어난 경도와 인성, 내마모성으로 인해 국방, 항공우주, 자동차, 선박, 석유화학, 채광, 전자, 임업 등 많은 제조업 분야에서 널리 사용되는 대표적인 구조재료 중의 하나이다. WC-Co 복합소재의 원재료인 텅스텐의 전략적인 가치로 인해 WC-Co 복합소재의 기계적 특성과 수명 향상시키기 위해서 많은 연구자들이 지난 수십 년간 미세구조의 나노화를 위한 많은 연구들을 진행해왔다. 이러한 노력에도 불구하고 나노 WC-Co 복합소재를 대량생산할 수 있는 방법은 아직까지 보고되지 않고 있다. 현재의 양산형 나노 WC-Co 복합소재의 평균입도 값은 대략 200 nm 로 보고되고 있다. 우리는 이 논문에서 해당 소재 제조의 첫 단계인 분말 합성부터 마감단계인 소결까지의 전 공정에 대한 연구를 통해 진정한 나노구조를 갖는 WC-Co 복합소재의 양산 가능성을 제시하고자 하였다.

우선 분말합성과정에서 일어나는 반응과 반응물의 입자성장 과정을 실험과 이론적 접근을 통하여 체계적으로 분석하였다. 결과 반응물의 입자 사이즈가 작으면 작을수록 WC 합성은 더 빨리, 더 낮은 온도, 더 짧은 시간 안에 완료되는 것이 확인되었고 이 모든 과정은 모두 구성 물질들의 확산에 의해서 제어된다는 것이 밝혀졌다. 우리는 이러한 사실들에 근거하여 분말합성의 승온과정을 제어함으로써 평균입도 10.54 nm, 입도 표준편차 2.1 nm 의 WC 나노분말을 합성하는 데 성공하였으며 반응물의 입자성장 제어에 의한 새로운 나노분말 합성법을 제안하였다.

다음으로 우리는 액상소결과정에 일어나는 심각한 입성장을 억제하는 방법으로 VC 도핑법을 사용하였으며, 실험적 이론적 접근을 통하여 소결과정에 일어나는 VC-doped WC-Co 시스템의 입성장 거동을 밝혀냈다. 소결과정 중 WC-Co의 입자성장은 주로 2차원 핵생성 (2-D nucleation) 후 성장의 기구를 통해서 일어났다. 또한 VC의 도핑은 WC 입자의 표면에 얇은 (V,W)C 박막을 형성시킴으로써 해당시스템의 2차원 핵생성의 장벽 (2-D nucleation barrier)을 높여주고 W 원자의 확산을 느리게 하는 것이 확인되었다.

이러한 사실에 근거하여 우리는 1300 °C의 고온에서 상당히 높은 열적 안정성을 가지는 나노구조의 WC-Co 복합소재 (평균입도 20~30 nm)를 개발하는 데 성공하였다. 이와 같은 나노구조의 높은 열적 안정성은 해당소재의 양산 가능성을 담보하는 중요한 지표이다.

주요어 : 나노구조, 세멘티드 카바이드, 입성장억제, 나노구조의 쌍결정 형성, 고분해능 투과전자현미경

학 번 : 2010-24047

List of Further Works

We found out that the heating stage of carbothermal reduction is very important for the synthesis of carbide nanopowder. Although we succeeded for the production of WC nanopowder with an extremely fine grain size, the effects of the environment during carbothermal reduction process such as CO/CO₂ gas pressure in a vacuum furnace are not explored. Therefore, more research about these issues are needed.

In addition, it was found that the nanostructured VC-doped WC-Co has a very high stability at high temperature for a long time. However, the full densification of nanostructured VC-doped WC-Co are not done yet. The effect of carbon contents in the system was not elucidated even though it is closely related to the growth behavior of WC during liquid phase sintering.

